

Interface-resolved DNS of vertical particulate channel flow in the turbulent regime

Markus Uhlmann*

Modeling and Numerical Simulation Unit
CIEMAT, 28040 Madrid, Spain

9 May 2008

Abstract

We have conducted a direct numerical simulation (DNS) study of dilute turbulent particulate flow in a vertical plane channel, considering thousands of finite-size rigid particles with resolved phase interfaces. The particle diameter corresponds to approximately 11 wall units and their terminal Reynolds number is set to 136. The fluid flow with bulk Reynolds number 2700 is directed upward, which maintains the particles suspended upon average. Two density ratios were simulated, differing by a factor of 4.5. The corresponding Stokes numbers of the two flow cases were $\mathcal{O}(10)$ in the near-wall region and $\mathcal{O}(1)$ in the outer flow. We have observed the formation of large-scale elongated streak-like structures with streamwise dimensions of the order of 8 channel half-widths and cross-stream dimensions of the order of one half-width. At the same time, we have found no evidence of significant formation of particle clusters, which suggests that the large structures are due to an intrinsic instability of the flow, triggered by the presence of the particles. It was found that the mean fluid velocity profile tends towards a concave shape, and the turbulence intensity as well as the normal stress anisotropy are strongly increased. The effect of varying the Stokes number while maintaining the buoyancy, particle size and volume fraction constant was relatively weak.

1 Introduction

The flow of a suspension of solid particles through vertically-oriented channels, pipes or ducts occurs in a large number of industrial applications, such as fluidized beds, riser flows and pneumatic transport lines. One of the central questions raised by previous studies of these flows concerns the nature of the mutual interaction between the turbulent flow field and the motion of the dispersed particles.

Experimental investigations of vertical wall-bounded flow have revealed that the intensity of fluid velocity fluctuations can be substantially modified by the addition of even a relatively small volume fraction of heavy particles (e.g. Tsuji, Morikawa, and Shiomi, 1984; Rogers and Eaton, 1990; Kulick, Fessler, and Eaton, 1994; Suzuki, Ikenoya, and Kasagi, 2000; Sato, Fukuichi, and Hichida, 2000; Hadinoto, Jones, Yurteri, and Curtis, 2005). Depending on the values of the various parameters, either enhancement or attenuation of the turbulence intensity is observed. In general the turbulence modulation effect can be attributed to a competition between two opposing mechanisms: dissipation in the vicinity of particles, and generation of velocity fluctuations due to wake shedding (Hetsroni, 1989). In addition to these direct consequences, particles can also indirectly affect the overall turbulent kinetic energy budget by interacting with specific coherent flow structures, thereby changing the very structure of the turbulent flow field. Indeed, it has been experimentally observed that small particles exhibit so-called 'preferential concentration', e.g. in vertical channel flow (Fessler, Kulick, and Eaton, 1994) and homogeneous isotropic turbulence

*Email: markus.uhlmann@kit.edu

(Aliseda, Cartellier, Hainaux, and Lasheras, 2002; Wood, Hwang, and Eaton, 2005). Maxey (1987) has shown that the accumulation generally occurs in regions of low vorticity and high strain rate. This feature was later confirmed by various DNS studies using the point-particle approach (Squires and Eaton, 1990; Wang and Maxey, 1993; Pan and Banerjee, 1996; Rouson and Eaton, 2001; Ahmed and Elghobashi, 2001; Marchioli and Soldati, 2002).

In 'two-way coupled' point particle simulations the hydrodynamic force acting upon the particles is fed back to the fluid, thereby allowing for the description of the influence of dispersed particles upon the carrier phase. Using this methodology, some of the mechanisms of turbulence modulation through local accumulations of particles has been elucidated in wall-bounded shear flow (Pan and Banerjee, 1996), homogeneous shear flow (Ahmed and Elghobashi, 2000) and homogeneous isotropic turbulence (Squires and Eaton, 1990; Sundaram and Collins, 1999; Ferrante and Elghobashi, 2003). It should be underlined, however, that most of the aforementioned results on 'preferential concentration' effects were obtained for particles whose diameter is smaller than the smallest flow scales, and for small values of the Reynolds number of the flow around individual particles (see also the review by Eaton and Fessler, 1994).

A different type of mechanism can lead to the formation of particle agglomerations when the particle Reynolds number attains values of $\mathcal{O}(100)$. In this regime, where the point-particle approach loses its validity, resolved DNS of the sedimentation of finite-size particles in ambient fluid (Kajishima and Takiguchi, 2002; Kajishima, 2004) has revealed that above a critical particle Reynolds number of approximately 300, particles tend to form clusters which are elongated in the direction of gravity. These clusters have a collective settling velocity exceeding that of an isolated particle, thereby inducing flow perturbations at length scales much larger than the particle diameter. Kajishima (2004) has also shown that angular particle motion plays an important role in the regeneration cycle of the agglomerations. Elongated particle accumulations were also reported by Nishino and Matsushita (2004) in experiments on grid-generated turbulence with particle diameters corresponding to 2-3 Kolmogorov length scales and particle Reynolds numbers in the range of 140-210. The formation of these clusters has been attributed to the effect of wake attraction, which is the result of a reduced drag force acting on a sphere located inside another sphere's wake. The variation of drag and lift experienced by pairs of spheres in different arrangements has been thoroughly investigated while keeping the solid objects fixed (Tsuji, Morikawa, and Terashima, 1982; Tsuji, Morikawa, and Fujiwara, 1985; Kim, Elghobashi, and Sirignano, 1993; Zhu, Liang, and Fan, 1994). When considering a pair of mobile particles which are settling under the effect of gravity after initially being vertically separated, the lower drag of the trailing sphere leads to an approach of the particles ('drafting'), a subsequent particle encounter ('kissing') and finally a lateral separation ('tumbling'), yielding a side-by-side arrangement (cf. Wu and Manasseh, 1998). Similar particle behavior due to wake effects has been identified in fluidization experiments involving many spheres (Fortes, Joseph, and Lundgren, 1987).

Despite considerable progress in the study of dispersed two-phase flows, a full understanding of the mechanisms driving the interaction between the fluid and solid phases is still lacking at the present date, especially in the regime where the smallest length scales of the turbulent flow are comparable to the particle diameter. In part this is due to the difficulties which are encountered in both laboratory and numerical experiments involving suspension flow, leading to a relative scarcity of detailed data. Concerning fully-resolved direct numerical simulations, the challenge lies in the fact that all relevant flow scales (pertaining to the flow around the particles and the background turbulence) need to be accurately represented, while at the same time imposing the appropriate boundary conditions at the moving phase interfaces.

High-resolution numerical studies of finite-size particles interacting with turbulence have often focussed on individual spheres. Kim, Elghobashi, and Sirignano (1998) have analyzed a mobile spherical particle in synthetic unsteady flow; Bagchi and Balachandar (2003, 2004) have considered a fixed particle swept by a homogeneous-isotropic turbulent field; Burton and Eaton (2005) have studied the interaction between a fixed particle and homogeneous-isotropic turbulence; Zeng, Balachandar, Fischer, and Najjar (2007) have determined the effect of wall-bounded turbulence upon the flow around a fixed particle. These investigations have provided highly detailed data on the time-dependent hydrodynamic forces acting upon a single particle in unsteady or turbulent

flow conditions; in the case of Burton and Eaton (2005) the effect of the presence of the particle upon the carrier phase was also evaluated. However, true particle mobility while allowing for collective effects could not be simulated with these approaches.

To our knowledge, the only previous direct numerical simulation study of turbulent vertical channel flow with finite-size mobile particles has been performed by Kajishima, Takiguchi, Hamasaki, and Miyake (2001). However, these authors considered only a small number (36) of relatively large particles (with a diameter corresponding to 32 wall units) and the angular particle motion was neglected. It should be mentioned that Pan and Banerjee (1997) have conducted resolved DNS of turbulent particulate flow in a horizontal open channel. They considered up to 160 stationary and mobile particles, the particle Reynolds number being $\mathcal{O}(10)$ in the latter case. Ten Cate, Derksen, Portella, and Van Den Akker (2004) have performed resolved DNS including a dense suspension of finite-size particles (solid volume fraction up to 10^{-1}) in forced homogeneous-isotropic turbulence. The particle Reynolds number in their case was $\mathcal{O}(10)$, precluding significant wake effects.

The aim of the present study is first and foremost to generate a body of detailed data describing the structure of the carrier phase as well as the motion of the dispersed phase in turbulent wall-bounded flow. For this purpose we have performed interface-resolved DNS of turbulent flow in a vertical plane channel configuration involving several thousand spherical particles and integrating the equations of motion over $\mathcal{O}(100)$ bulk flow time units. The parameters are chosen such that the mean particle Reynolds number is 136, which means that significant wake effects can be expected. The specific questions which we will address concern on the one hand the occurrence of preferential concentration of the solid phase, and on the other hand the possible formation of particle-induced flow structures.

The outline of this article is as follows. In the following section the numerical method employed in our simulations is explained. We report the various validation checks and grid convergence tests which have been performed, specify the conditions of the simulated flow cases and describe the initialization procedure. In § 3 we focus on the Eulerian statistics. The procedure for computing the statistical quantities and their convergence is described in detail. We discuss the results for Eulerian one-point moments and probability density functions of both phases before turning to the Lagrangian statistics in § 4. The spatial structure of the dispersed phase is analyzed in § 5 and the occurrence of new coherent flow structures is investigated in § 6. The paper closes with a short summary and discussion.

2 Numerical method

It has been recognized for some time that DNS of particulate flows can be efficiently performed on computational meshes which are fixed in space and time, while solving a single set of equations in the entire domain, i.e. including the space occupied by the solid bodies (Höfler and Schwarzer, 2000; Glowinski, Pan, Hesla, Joseph, and Périaux, 2001; Kajishima and Takiguchi, 2002). In this framework, various techniques have been used by different authors in order to impose the constraint of rigid body motion upon the fluid at the particle locations.

Our present simulations have been carried out with the aid of a variant of the immersed boundary technique (Peskin, 1972, 2002) proposed by Uhlmann (2005a). This method employs a direct forcing approach, where a localized volume force term is added to the momentum equations. The additional forcing term is explicitly computed at each time step as a function of the desired particle positions and velocities, without recurring to a feed-back procedure; thereby, the stability characteristics of the underlying Navier-Stokes solver are maintained in the presence of particles, allowing for relatively large time steps. The necessary interpolation of variable values from Eulerian grid positions to particle-related Lagrangian positions (and the inverse operation of spreading the computed force terms back to the Eulerian grid) are performed by means of the regularized delta function approach of Peskin (1972, 2002). This procedure yields a smooth temporal variation of the hydrodynamic forces acting on individual particles while these are in arbitrary motion with respect to the fixed grid.

Since particles are free to visit any point in the computational domain and in order to ensure that the regularized delta function verifies important identities (such as the conservation of the total force and torque during interpolation and spreading), a Cartesian grid with uniform isotropic mesh width $\Delta x = \Delta y = \Delta z$ is employed. For reasons of efficiency, forcing is only applied to the surface of the spheres, leaving the flow field inside the particles to develop freely. Fadlun, Verzicco, Orlandi, and Mohd-Yusof (2000) have demonstrated that the external flow is essentially unchanged by this procedure; in Uhlmann (2005b) it was confirmed that the impact upon the particle motion is indeed small. Figure 1 shows the distribution of forcing points on the surface of a sphere with diameter $D/\Delta x = 12.8$ and the corresponding Eulerian grid in the vicinity.

The immersed boundary technique of Uhlmann (2005a) is implemented in a standard fractional-step method for incompressible flow. The temporal discretization is semi-implicit, based on the Crank-Nicholson scheme for the viscous terms and a low-storage three-step Runge-Kutta procedure for the non-linear part (Verzicco and Orlandi, 1996). The spatial operators are evaluated by central finite-differences on a staggered grid. The temporal and spatial accuracy of this scheme are of second order.

The particle motion is determined by the Runge-Kutta-discretized Newton equations for translational and rotational rigid-body motion, which are explicitly coupled to the fluid equations. The hydrodynamic forces acting upon a particle are readily obtained by summing the additional volume forcing term over all discrete forcing points and multiplying the result by a factor of -1 . Thereby, the exchange of momentum between the two phases cancels out identically and no spurious contributions are generated. The analogue procedure is applied for the computation of the hydrodynamic torque driving the angular particle motion.

During the course of a simulation, particles can approach each other closely. However, very thin inter-particle films cannot be resolved by a typical grid and therefore the correct build-up of repulsive pressure is not captured which in turn can lead to possible partial ‘overlap’ of the particle positions in the numerical computation. In practice, we use the artificial repulsion potential of Glowinski, Pan, Hesla, and Joseph (1999), relying upon a short-range repulsion force (with a range of $2\Delta x$), in order to prevent such non-physical situations. Essentially the same method is used for the treatment of particles approaching solid walls. The stiffness parameter appearing in the above mentioned authors’ definition of the repulsion force has been set to $\epsilon_p = 8 \cdot 10^{-4} D / (\rho_f u_{c,\infty}^2)$ (where $u_{c,\infty}$ is the terminal particle settling velocity in ambient fluid), based on calibration in simulations of two sedimenting particles and particle-wall interactions. It should be noted that the use of an approximate treatment of particle ‘collisions’ somehow taints an otherwise ‘direct’ numerical simulation method. It is also true that the details of individual particle encounters sometimes depend on the method for the collision treatment, e.g. in the highly unstable case of ‘drafting-kissing-tumbling’ of two particles (Glowinski et al., 2001). However, when considering dilute suspensions particle collisions are expected to occur so infrequently that representing their exact dynamics does not seem vital for a faithful description of the flow. Previous simulations incorporating the method of Glowinski et al. (1999) have demonstrated that a very good agreement with experimental measurements can be achieved even in a relatively dense system (Pan, Joseph, Bai, Glowinski, and Sarin, 2002).

2.1 Validation and grid convergence

The present numerical method has been submitted to exhaustive validation tests (Uhlmann, 2004, 2005a,b, 2006a). These tests have established the following features: (i) second-order accuracy of the interpolation scheme and low sensitivity of the error with respect to the position of the immersed object relative to the grid; (ii) favorable smoothness properties of the scheme in computations involving oscillating objects.

In addition, we have performed a detailed grid convergence study of the motion of particles in pressure-driven vertical plane channel flow (Uhlmann, 2006b). Two regimes were considered: laminar flow with a single heavy particle of diameter $D/h = 1/20$ (h being the channel half width) at $Re_{D,\infty}=100$ and turbulent flow with four identical particles at $Re_{D,\infty}=136$ (the terminal Reynolds number $Re_{D,\infty}$ is based upon the particle diameter and the terminal settling velocity in

ambient fluid). In the former case, four different grids were considered, corresponding to a particle resolution of $D/\Delta x = \{12.8, 19.2, 25.6, 38.4\}$, while the CFL number was kept constant. Second order convergence of the particle velocities was observed in this test. In the turbulent case, the flow conditions were chosen equal to those of the configuration of interest in the following section (cf. case B of table 1 and 2). Three spatial resolutions, $D/\Delta x = \{12.8, 19.2, 25.6\}$, were analyzed in a computational domain which was sufficiently large to allow for sustenance of the turbulent state. During the observation interval of approximately 3.6 bulk flow time units, all three grids yield the same flow features. The instantaneous particle velocities obtained from the coarsest and the finest grid match to within 8.3% of the terminal velocity; the second-moment fluid statistics exhibit a maximum relative discrepancy of 7%. It should be noted that particle paths computed with two different spatial resolutions will invariably deviate with time (even when both simulations are extremely well resolved) since perturbations can be amplified under supercritical (i.e. turbulent) conditions. From these considerations and the above mentioned comparison with experimental data for sedimentation of a single sphere, it was concluded that a resolution of $D/\Delta x = 12.8$ is sufficient for our present investigation of turbulent particulate channel flow. Figure 1 shows this grid in the vicinity of a sphere.

In separate simulations it was verified that our DNS code reproduces single-phase turbulence results for plane channel flow faithfully. In particular, using a mesh width of $\Delta x/h = 1/256$ (which corresponds to the value chosen in the following section) gives results in very good agreement with the reference data of Kim, Moin, and Moser (1987). The mean velocity profile from our single-phase computation has been included in figure 6(b).

2.2 Flow configuration

We are considering particulate flow in a plane channel which is aligned along the gravitational (x) direction (y is the wall-normal and z the spanwise coordinate, cf. figure 2). The fluid is driven upwards by a mean pressure gradient $\langle p \rangle_{,x} < 0$. The computational domain is periodic in the streamwise and spanwise directions (with periods L_x and L_z), i.e. particles leaving the domain on any of the four periodic end-planes re-enter at the opposite side. At the solid walls, the no-slip condition is imposed upon the fluid, while the particles rebound due to the short-range repulsion force, as specified in §2. The bulk flow Reynolds number is maintained constant at a value of $Re_b = u_b h/\nu = 2700$ (u_b being the bulk velocity and ν the kinematic viscosity), which generates a turbulent flow with $Re_\tau = u_\tau h/\nu \approx 172$ (u_τ being the wall shear velocity) in the absence of particles. The particle diameter is chosen as $D/h = 1/20$, corresponding to $D^+ = Du_\tau/\nu = 8.6$ in wall units of the unladen flow (11.25 wall units of the laden flow). Physically, this regime of particle sizes is interesting, since the particle diameter is comparable to the cross-stream length scales of coherent structures typically found in the buffer layer of wall-bounded turbulent flow; a mutual interaction can therefore be expected. Numerically, this particle size is the smallest value for which we can accurately represent the local flow at a particle Reynolds number of $\mathcal{O}(100)$ on the grid required for an accurate computation of the single-phase turbulence. As mentioned in the previous section, we choose a spatial resolution of $D/\Delta x = 12.8$, which corresponds to a mesh width of $\Delta x/h = 1/256$, i.e. $\Delta x^+ = 0.67$ in wall units. The time step for case A (the two flow cases are further specified below) was set to $\Delta t = 0.5761\Delta x/u_b$, which corresponds to a maximum CFL number of approximately 1; for case B the step was reduced to $\Delta t = 0.4148\Delta x/u_b$, i.e. a maximum CFL number of approximately 0.75.

We have set the bulk fluid velocity (u_b) equal to the terminal particle velocity ($u_{c,\infty}$). This condition means that the average vertical velocity of the particles will be close to zero, supposing that their average wall-normal spatial distribution is near uniform and neglecting wall effects, collective effects and possible effects arising from the interaction with turbulence. With these settings it turns out that the vertical velocity averaged over all particles takes a slightly positive value as we will see below. From the condition $u_{c,\infty}=u_b$ it follows that the terminal particle Reynolds number measures $Re_{D,\infty} \approx 136$. From the equality between buoyancy and drag forces acting upon an isolated particle, we can form the Archimedes number, which takes the following

value:

$$Ar = (D/h)^3 Re_b^2 \frac{|g_x|h}{u_b^2} \left(\frac{\rho_p}{\rho_f} - 1 \right) = 13328, \quad (1)$$

where ρ_p/ρ_f is the density ratio between particle and fluid and $\mathbf{g} = (g_x, 0, 0)$ the vector of gravitational acceleration (with $g_x < 0$). This leaves us with one parameter free to choose (ρ_p/ρ_f , say), the other one ($|g_x|h/u_b^2$) being fixed by (1).

We have analyzed two cases with parameter values as given in table 1. The current range of density ratios is representative of the motion of glass, ceramics or sand in water and is often investigated in laboratory experiments (e.g. Parthasarathy and Faeth, 1990; Suzuki et al., 2000; Kiger and Pan, 2002). Apart from its relevance for the study of fundamental questions in turbulence-particle interaction, this regime has important applications in environmental flows and hydrology. The relative particle density in case A is approximately 4.5 times higher than in case B, and the Stokes number (defined as the ratio between particle and fluid time scales) varies accordingly. In particular, we determine the particle time scale from the usual Stokes drag law, $\tau_{SD} = D^2\rho_p/(18\nu\rho_f)$, and consider two time scales for the fluid motion: the near-wall scale $\tau^+ = \nu/u_\tau^2$ and the bulk flow scale $\tau_b = h/u_b$. Consequently, we can form two Stokes numbers, characterizing the ratio of time scales in the near-wall region, $St^+ = \tau_{SD}/\tau^+$, and in the outer flow $St_b = \tau_{SD}/\tau_b$. Table 1 shows that the present particles have a relatively large response time with respect to the flow in the near-wall region, where $St^+ > 10$, but the scales of both phases are comparable in the bulk of the flow, i.e. $St_b \sim \mathcal{O}(1)$.

The global solid volume fraction has been set to $\Phi_s = 0.0042$, which can be considered at the upper limit of the dilute regime.

The two cases were run in computational domains of different wall-parallel dimensions, the volume in case B being eight times larger ($4h \times 2h \times 1h$ versus $8h \times 2h \times 4h$). The number of particles in cases A, B is therefore $N_p = \{512, 4096\}$, respectively. The domain used in case A evidently constitutes a smaller sample size per instantaneous flow field. However, it allows for simulations over longer time intervals which is of special interest for the computation of slowly evolving statistical quantities acquired along the particle paths. Table 2 shows the global grid size of the simulations, which exceeds 10^9 Eulerian nodes and $2 \cdot 10^6$ Lagrangian force points in case B, where the work is typically distributed over 512 PowerPC processors with fiberoptical interconnect (MareNostrum at BSC-CNS, Barcelona). It should be mentioned that the simulation of case B has required roughly 10^6 CPU hours of execution time.

2.3 Initialization of the simulations

Particles are introduced into fully-developed turbulent single-phase flow at time t_0 . The initial particle positions form a regular array covering the computational domain, perturbed randomly with an amplitude of one particle diameter. Their initial velocities are matched with the fluid velocities found at t_0 at the locations of each particle's center; the initial angular particle velocities are set to zero. During the first time step of the two-phase computation, the coupling algorithm solidifies the fluid occupying the volume of each particle and buoyancy forces set in. Figure 3(a) shows how the average over all particles of the vertical particle velocity drops from a value close to the bulk fluid velocity to almost zero over an initial interval of approximately 3 (1) bulk time units in case A (B). Let us mention that the long-time averaged mean upward drift of the particles amounts to $0.029u_b$ and $0.058u_b$, respectively. The data corresponding to the initial transient will not be considered in the following and, therefore, an initial interval of 17 bulk time units has been discarded. The length of the observation interval for the two cases is indicated in table 2.

From figure 3(b) it can be seen that the friction velocity increases immediately after the addition of particles, leading to a sharp rise of Re_τ which then oscillates around a new mean value of approximately 225 in both cases. The amplitude and frequency of the oscillations is larger in case A due to the smaller box size. This higher friction velocity in the particulate cases reflects the modification of the mean fluid velocity profile as discussed below (cf. figure 6). From here on, it is understood that quantities given in wall units (indicated by the usual superscript '+') are

normalized with the actual friction velocity, i.e. the increased values are used in the particulate flow cases.

3 Eulerian statistics

3.1 Computation and convergence of statistical quantities

Let us introduce the notation for the different averaging operations employed in the following. $\langle \xi \rangle_x$ refers to the streamwise average of a quantity ξ , $\langle \xi \rangle_{xz}$ is the average over wall-parallel planes and $\langle \xi \rangle_t$ is the temporal average (over the observation interval given in table 2); the average over time and wall-parallel planes is denoted by $\langle \xi \rangle = \langle \langle \xi \rangle_{xz} \rangle_t$; finally, $\langle \xi \rangle_p$ refers to the instantaneous ensemble average over all particles.

The Eulerian space averages of quantities related to the dispersed phase are carried out for discrete bins in the wall-normal direction, defined as $I_{yj} = [j - 1, j) \cdot 2h/N_{bin} \forall 1 \leq j \leq N_{bin}$. In practice a value of $N_{bin} = 80$ was chosen (except where otherwise stated), such that the width of each bin corresponds to one particle radius.

The time- and plane-averaged number density is then computed for each bin by the following formula:

$$\langle n_s \rangle(y_j) = \frac{1}{n_{obs} L_x L_z |I_{yj}|} \sum_{l=1}^{n_{obs}} \sum_{\substack{i=1 \\ y_c^{(i)}(t_l) \in I_{yj}}}^{N_p} 1, \quad (2)$$

where $\mathbf{x}_c^{(i)} = (x_c^{(i)}, y_c^{(i)}, x_c^{(i)})$ are the center coordinates of the i th particle, y_j is the coordinate of the center of the bin I_{yj} , n_{obs} the number of available records during the observation interval and $|I_{yj}|$ is the width of j th wall-normal interval. The solid volume fraction simply becomes:

$$\langle \phi_s \rangle(y_j) = V_c \langle n_s \rangle(y_j), \quad (3)$$

denoting the particle volume by $V_c = D^3 \pi / 6$.

The time- and plane-wise average of a quantity ξ_c is computed as follows:

$$\langle \xi_c \rangle(y_j) = \frac{1}{\langle n_s \rangle(y_j) n_{obs} L_x L_z |I_{yj}|} \sum_{l=1}^{n_{obs}} \sum_{\substack{i=1 \\ y_c^{(i)}(t_l) \in I_{yj}}}^{N_p} \xi_c^{(i)}(t_l). \quad (4)$$

Here ξ_c can stand for any component of the linear or angular particle velocity vectors, which are denoted by $\mathbf{u}_c^{(i)}$ and $\boldsymbol{\omega}_c^{(i)}$, respectively.

In order to analyze the motion of the dispersed phase, we have stored the full set of particle-related quantities after every 10 (5) time steps for case A (B); this corresponds to approximately $1.5 \cdot 10^7$ ($5.2 \cdot 10^7$) samples. Statistical quantities were then computed in a post-processing stage.

In the vicinity of sharp gradients, discrete binning of the data for the dispersed phase tends to smooth out the profiles. This effect can be seen in figure 4(a), where the solid volume fraction of case B is shown for different numbers of wall-normal bins varying from $N_{bin} = 40$ to 320. The plot confirms the adequacy of the overall number of discrete samples, because the profile of $\langle \phi_s \rangle$ does not become significantly more noisy when increasing the number of bins. Since the particles have a non-negligible size with respect to the channel width ($D/h = 1/20$), the apparent drop from the maximum to a value of zero at the wall could be an artifact of the binning. Figure 4(b) demonstrates that this is not the case. Using fine bins with a width of $D/8$ reveals first that there are no particles within $y_c \leq D/2$, which is the zone ‘forbidden’ by the geometric constraint of the wall. Secondly it shows that the solid volume fraction smoothly increases for wall-distances larger than this lower limit. Furthermore, let us point out that the mean wall-normal particle velocity is negligible ($\max |\langle v_c \rangle| / u_b \leq \{10^{-4}, 7 \cdot 10^{-4}\}$ in cases A, B), indicating that the particle distribution has indeed achieved a statistically steady state.

Concerning the statistics of the carrier phase, we have accumulated the usual low-order one-point moments (mean velocity, stress tensor) during the simulations. For this purpose, averaging was performed over the entire composite flow field, i.e. containing the regions of the immersed solid particles (the average velocity obtained by this procedure is denoted by $\langle u \rangle$ etc). This decision was taken in favor of computational efficiency, and its consequences are discussed below. On the other hand, we have stored a number of full instantaneous flow fields and corresponding particle data for visualization purposes and *a posteriori* computation of additional quantities, such as two-point correlation functions. From these fields we have estimated the difference between averaging first and second moments over the composite field versus taking into account the actual fluid nodes only; the fluid-only averaged velocity is denoted by $\langle u \rangle_f$. For more details the reader is referred to appendix A. This test has lead us to the conclusion that the employed method overestimates the streamwise velocity fluctuations (by up to 6.7%) and slightly underestimates the mean fluid velocity (by less than 0.7%); the wall-normal fluctuation and the Reynolds stress are overestimated by approximately 2%, the spanwise component by 0.7%. These differences affect the data presented in some of the figures discussed in the present section as well as the following section § 3.2 (i.e. the figures 5, 6, 9, 10b, 11, 12, 13b). As shown in appendix A, the over-prediction of the streamwise velocity fluctuation amplitude can be quite accurately represented by a linear function of the solid volume fraction, allowing for a correction of the run-time statistics. This correction has been included in figures 11, 12 and 13(b).

The usual check of the statistical convergence of low-order moments in single-phase plane channel flow includes a verification of the linearity of the total shear stress profile. In the multi-phase case, however, the streamwise momentum balance includes an additional contribution. The equation, as derived in appendix B, reads:

$$\frac{d\langle u'v' \rangle^+}{d\bar{y}} - \frac{1}{Re_\tau} \frac{d^2\langle u \rangle^+}{d\bar{y}^2} + \left(\frac{\rho_p}{\rho_f} - 1 \right) \frac{g_x h}{u_\tau^2} (\Phi_s - \langle \phi_s \rangle) = 1, \quad (5)$$

where $\bar{y} = y/h$, and (u', v', w') are the components of the fluctuations with respect to the mean velocity $(\langle u \rangle, 0, 0)$. It should be noted that this equation is written for the composite flow field (including the fluid located at the positions of the solid particles), and all averaging operators extend over the entire computational domain Ω . It can be seen from (5) that whenever the particle distribution is not uniform (i.e. when $\Phi_s - \langle \phi_s \rangle$ is different from zero), the total shear stress does not vary linearly with the wall-distance. In order to test whether the accumulated data has indeed achieved statistical equilibrium, we have compared the terms of the integral of equation (5), viz.

$$\underbrace{\langle u'v' \rangle^+ - \frac{1}{Re_\tau} \frac{d\langle u \rangle^+}{d\bar{y}}}_{\tau_{tot}} + \underbrace{\left(\frac{\rho_p}{\rho_f} - 1 \right) \frac{g_x h}{u_\tau^2} \int (\Phi_s - \langle \phi_s \rangle) d\bar{y}}_{I_\phi} = \bar{y} - 1. \quad (6)$$

In practice, the integral of the solid volume fraction was evaluated numerically (after piecewise polynomial interpolation of the statistical data, using cubic spline functions). Figure 5(a-b) shows the different contributions to the balance (6). It can be seen that the profile of τ_{tot} deviates quite significantly from the usual straight line, the particle contribution I_ϕ being significant at all wall-distances. However, the sum of the stress terms and the particle contribution $\tau_{tot} + I_\phi$ does indeed follow the line $\bar{y} - 1$ quite closely. It is further observed that the data in figure 5(a-b) does not verify the odd symmetry with respect to the center at $\bar{y} = 1$ as much as would be expected from the length of the respective observation intervals and the size of the computational boxes. We will return to this lack of symmetry in § 6 below. Additional averaging over both channel halves clearly improves the match (cf. figure 5c-d). Due to the larger sample size (both for the carrier phase as well as the dispersed phase), the statistical data for case B is found to be closer to statistical equilibrium than case A. Therefore, in the following we will mainly discuss results from case B. It should be noted that in both cases, a certain deviation from linearity is observed in a limited region near the wall ($\bar{y} \leq 0.1$). This discrepancy can be attributed to the effect of

discrete binning of the solid volume fraction, as discussed above (cf. figure 4a). Finally, it can be concluded that the statistical data—when averaged over both channel halves—has approximately achieved a steady state consistent with equation (6).

3.2 One-point moments

The mean fluid velocity profiles (computed by averaging over the composite flow field) normalized by the bulk velocity are shown in figure 6(a). We observe a clear difference with respect to the single-phase case, characterized by a tendency of the particulate flow to form a concave profile with higher gradients at the walls and a flat section near the center of the channel. The concave shape is slightly more pronounced in the high-inertia case A. On the other hand, when normalized in wall units (cf. figure 6b), the particulate flow cases exhibit a considerably lower mean velocity than the single-phase counterpart across the whole channel. As expressed by the streamwise momentum balance equation (5) the mean velocity of the composite field is determined by the Reynolds shear stress and the particle distribution. Before turning to the discussion of these two quantities, let us mention that concave mean velocity profiles have previously been observed in experiments on dilute particulate flow at various parameter points: in vertical pipes (Tsuji et al., 1984; Hadinoto et al., 2005) and—to a lesser extent—in vertical channels (Sato et al., 2000). However, neither the distribution of the solid volume fraction nor the Reynolds shear stress profiles are available from these experimental data-sets.

The profiles of the mean solid volume fraction are shown in figure 7. In both cases we observe a sharp peak at a wall distance of approximately 16 wall units ($\bar{y} = 0.07$), a slightly below-average value around $\bar{y} = 0.2$ and finally a mild local maximum at the center of the channel. A sharp rise of the solid volume fraction near the wall was also reported by Suzuki, Ikenoya, and Kasagi (2000) in their experiment on downward channel flow containing particles with a diameter of approximately 4 wall units.

A number of mechanisms which influence the wall-normal distribution of particles have been discussed in the literature. One of the principal contributions has been termed *turbophoresis* (Caporaloni et al., 1975; Reeks, 1983), referring to an average migration of particles in the direction opposite to gradients in the turbulence intensity. For an individual particle this means that it is less probable to receive the necessary momentum driving it from a region of low turbulence intensity towards a high-intensity region than vice versa; turbophoresis is then a statistical consequence. An expression corresponding to a turbophoretic force appears formally when considering a Eulerian formulation for the dispersed phase. In this context the wall-normal particle momentum equation contains the following term: $-\partial\langle v'_c v'_c \rangle / \partial y$ (Young and Leeming, 1997). The profile of this quantity is shown in figure 8 (the correlation $\langle v'_c v'_c \rangle$ itself is shown in figure 13 and will be discussed below). It can be seen that the turbophoresis term is positive for wall-distances below $y_c^+ \approx 16$ (i.e. driving particles towards the center) and then negative (directed wall-ward) up to approximately $\bar{y} = 0.2$; for larger wall-distances its values are close to zero. The point where the turbophoretic force changes sign corresponds to the near-wall maximum of the mean solid volume fraction $\langle \phi_s \rangle$ (cf. figure 7), and the interval over which the force has significant values matches the region where the corresponding bump in $\langle \phi_s \rangle$ is observed. This close correspondence suggests that turbophoresis is indeed important for the mean wall-normal particle distribution in the presently investigated cases. Other effects—such as the mean shear-induced lift force and the turbulent diffusion—are expected to contribute as well. However, the additional mechanisms are not directly quantifiable from the available data, and, therefore, it is not possible to further investigate their relative importance in establishing the equilibrium distribution.

The Reynolds stress normalized by the friction velocity is shown in figure 9(a). The profiles of both simulated cases are of a much smaller amplitude than the single-phase reference data across most of the channel width. When normalized by the bulk velocity, the reduction is limited to wall-distances $\bar{y} \gtrsim 0.2$. Notably, near the center of the channel a considerable region with vanishing Reynolds stress is observed. This means that the correlation between the streamwise and the wall-normal fluid velocity fluctuations is significantly reduced in the present cases. However, the sum of the Reynolds shear stress and the contribution from the solid volume fraction to the integrated

momentum balance (6), i.e. $\langle u'v' \rangle^+ + I_\phi$, (shown in figure 9b) is of larger absolute value than the Reynolds shear stress of the single-phase flow when normalized in wall units. From equation (6) it follows then that the wall-normal gradient of the mean streamwise velocity (in wall units) is smaller in the particulate case, leading to the reduced value of $\langle u \rangle^+$ observed in figure 6(b). Furthermore, we note from figure 9(b) that the largest difference between the sum $\langle u'v' \rangle^+ + I_\phi$ and the Reynolds shear stress of the single-phase case is obtained around $\bar{y} = 0.075$, where the profile of the former quantity exhibits a visible bump. This is evidently the signature of the near-wall peak of the solid volume fraction (cf. figure 7) which is found at the same location. Consequently, the accumulation of particles in the buffer region has the effect of bringing more momentum towards the wall. This in turn causes the flattening of the mean velocity profile and generates a shear-free region near the center of the channel.

Figure 10(a) shows the profiles of the mean (streamwise) particle velocity, which is positive in the center of the channel and changes sign at approximately $\bar{y} = 0.2$. In both cases the shape of the profile is very similar to the corresponding mean fluid velocity profile (cf. figure 6a), but with a negative shift. Close to the wall, the mean particle velocity profile differs in shape from the fluid velocity counterpart, as will be discussed below. In figure 10(b) the difference between the mean velocities of the two phases, $\langle u_c \rangle - \langle u \rangle$, is plotted; it is found to be approximately constant and nearly equal to $-u_b$. For wall-distances $\bar{y} \leq 0.1$, however, the magnitude of the relative mean velocity substantially decreases. This result indicates that the coefficient of the drag force acting on average upon the particles in this region is higher than at large wall-distances. Similar behavior is reported by Zeng, Balachandar, and Fischer (2005) who have investigated the drag force on a single sphere translating in a channel with quiescent fluid. These authors have detected a significant increase of the drag coefficient for wall distances below $y/D = 2$ (i.e. for $\bar{y} \leq 0.1$ in the present context), at similar values for the particle Reynolds number. A drag coefficient based upon the relative mean velocity of our simulations can be computed by formulating the equilibrium between buoyancy and drag forces, $C_{D,present} = (\rho_p/\rho_f - 1)|g_x| \frac{4}{3}D/(\langle u_c \rangle - \langle u \rangle)^2$, and substituting the data of figure 10(b). The ratio between this relative mean DNS drag coefficient and the standard drag coefficient of an isolated sphere given by the Schiller-Naumann formula (Clift, Grace, and Weber, 1978) is $C_{D,present}/C_{D,SN} = 1.46$ at a wall distance of $y/D = 0.9375$ (where the particle Reynolds number based upon the relative mean velocity is 107.2). As a comparison, the value obtained from the correlation formula given by Zeng et al. (2005) is $C_{D,ZBF}/C_{D,SN} = 1.44$. The match is indeed remarkable, indicating that results obtained for the wall-effect on individual particles at ambient flow conditions are indeed relevant to turbulent particulate flow in the dilute regime.

The r.m.s. fluctuations of fluid velocities, normalized by the friction velocity, are shown in figure 11. This figure also includes profiles of the streamwise component from which the overestimation due to the computation of statistics over the composite flow field has been subtracted (using the fit of appendix A). The streamwise component in both particulate flow cases is strongly enhanced as compared to the single-phase flow, except for a small interval very close to the wall. The wall-normal component is slightly increased for $\bar{y} < 0.1$ and slightly decreased for wall-distances above that value; the spanwise component is decreased almost across the whole channel width. When normalized by the bulk velocity, all three profiles exceed the single-phase reference data, except for the spanwise component for intermediate wall-distances ($0.1 \leq \bar{y} \leq 0.6$). Since the streamwise component is dominant, the turbulent kinetic energy is significantly enhanced with respect to the single-phase flow, as shown in figure 12. When subtracting the overestimation due to the composite flow statistics, the ratio reaches approximately 4.6 (5.3) on the centerline in case A (B); when normalized in bulk units, the ratio is 7.9 (9.0). The principal reason for the observed turbulence enhancement is the generation of velocity fluctuations in the wakes trailing the particles. Wakes are indeed found to be the most prominent flow structures, as can be concluded from flow visualisations (cf. figure 26 below). The wake structures significantly increase the turbulence intensity, but they do not contribute to the generation of the mean Reynolds shear stress, since correlations between u' and v' internal to each wake cancel out upon averaging over an ensemble of mostly uncorrelated wakes (the random-like distribution of particles will indeed be confirmed in § 5). In addition to the wakes, new large-scale velocity structures representing streamwise velocity

perturbations appear in the particulate flow. These flow structures, which will be discussed in § 6, further contribute to the enhancement of turbulence intensity. In case A somewhat lower values for the streamwise turbulence intensity are obtained when compared to case B. This difference might be a consequence of the smaller domain size in the former case, where the large particle-induced structures are strongly constrained. A significant increase in streamwise velocity fluctuation levels has also been detected by Suzuki et al. (2000), although their solid volume fraction was one order of magnitude lower. The authors already attributed this observation to the presence of the wakes.

The r.m.s. velocity fluctuations of the dispersed phase are shown in figure 13(a); for convenience, a comparison of the r.m.s. velocity fluctuations of both phases in case B (i.e. combining data of figures 11 and 13a) is shown in figure 13(b). A similarity between the corresponding components of the two phases can be observed on these graphs, except for the immediate vicinity of the wall. The streamwise particle r.m.s. velocities also exhibit a mild peak in the buffer layer, and the shape of the wall-normal and spanwise components is similar as for the fluid data. This similarity shows that the present particles are able to respond to the fluid velocity fluctuations. The kinetic energy of the particle velocity fluctuations (not shown) is lower than the fluid turbulent kinetic energy across the whole channel. This behavior is expected due to the particle inertia. In the high-inertia case A, the intensity of the fluctuations of all particle velocity components is smaller than the fluid data. In case B, the streamwise component is also considerably smaller than the corresponding fluid values. The level of the remaining two components, however, slightly exceeds the fluid counterparts across most of the channel. In addition, it can be seen in figure 13 that the particle velocity fluctuation intensities flatten when approaching the wall and increase again for small wall-distances $\bar{y} \lesssim 0.06$ (corresponding to 14 wall units). What looks like a ‘kink’ of the curves is not an artifact of the data analysis, since a refinement of the width of the bins used in the computation of the Eulerian statistics has confirmed the observed trend. It should be remarked that the particles are not subject to the no-slip condition at the wall, and, therefore, the asymptotic behavior of the particle velocity is expected to differ from the one of the fluid velocity (cf. Kulick et al., 1994). However, it is difficult to imagine how the intensity of the fluctuation components can rise near the wall, where the flow is increasingly quiescent. Also, the observed behavior does not seem to be due to the numerical treatment of particle-wall collisions, since those only concern the wall-normal component of the particle motion, whereas the profiles of all components exhibit a similar upward trend. It must be concluded that the reasons for the increased near-wall variance of particle motion remain unclear at the time being, requiring further research.

The profiles of the spanwise component of the mean angular particle velocity $\langle \omega_{c,z} \rangle$ are shown in figure 14(a). In both cases there is a minimum at a wall-distance of approximately 25 wall units, and the profile tends towards zero at the centerline and at the wall. In figure 14(b) the DNS data are compared to the mean shear profile. In a linear shear flow the steady rotation of a cylinder is described by the formula $-A d\langle u \rangle / dy$, where A is positive and decreases with the shear Reynolds number (cf. Ding and Aidun, 2000; Zettner and Yoda, 2001). Constrained simulations of a single neutrally-buoyant and spherical particle placed in laminar pipe flow have likewise yielded a proportionality between the steady-state angular particle velocity and the wall-normal fluid velocity gradient over most of the pipe radius (Yang et al., 2005, figure 3). It can be seen in figure 14(b) that our data for case B are reasonably well represented when choosing $A = 0.1$, except for the region $y^+ < 25$ (similarly for case A, which is not shown). The discrepancy in the near-wall region can probably be attributed to a modification of the flow field around particles in the immediate vicinity of the wall induced by the no-slip condition. A similar tendency was observed for a cylinder in linear shear flow when the confinement ratio was lowered (Ding and Aidun, 2000).

3.3 Probability density functions and quadrant analysis

Probability density functions (pdfs) of the fluid velocity components were computed from 12 instantaneous flow fields of case B, taking into account only values at grid nodes inside the fluid domain. The sample size was doubled by making use of the symmetry with respect to the center of the channel. In the following we will discuss the normalized pdfs in the buffer region ($y^+ = 20$) and

at the center of the channel, in comparison to the single-phase data of Moser, Kim, and Mansour (1999) at $Re_\tau = 180$. The values of the skewness at these wall-distances are given in table 3. It can be seen that the skewness of the spanwise velocity component computed from our data set is close to zero as a consequence of the spanwise periodicity, indicating that sufficient sample has been obtained. In figures 15 and 16 we observe that the pdf for the streamwise component is strongly non-symmetric with respect to the mean value. While the branch for positive fluctuations matches those of the single-phase data closely, there exists a higher probability of finding strongly negative fluctuations in the present particulate case. This tendency is confirmed for both wall-distances and it reflects the negative perturbations induced by the streamwise momentum deficit in the wakes trailing the particles. The comparison with the single-phase data shows that the influence of the particles upon the shape of the pdfs for the wall-normal and spanwise velocity components is relatively small, manifesting itself through a small increase of the non-Gaussian tails. The skewness of the wall-normal component in the buffer layer is reduced from its value in single-phase flow.

The corresponding pdfs of the particle velocity are shown in figure 17 for different wall-distances (in the buffer region, the logarithmic layer and in the center of the channel); the skewness values are given in table 4. The curves for the streamwise component are found to largely resemble Gaussian functions. However, they exhibit discernible non-Gaussian tails on the negative side which grow with the wall-distance. This feature indicates that the particles respond to some degree to the negative fluid velocity fluctuations which they experience in the wakes of other particles. On the other hand, the pdfs for the wall-normal component are characterized by much more pronounced non-Gaussian tails. Additionally, in the buffer region one can observe a strong skewness of v'_c towards negative values, i.e. high-velocity motion (with intensity above four standard deviations) directed towards the wall is occurring more frequently than away from it. Since the pdf of wall-normal fluid velocity at the same wall-distance was not found to exhibit a comparable skewness (cf. figure 15b, comparison between tables 3 and 4), the present result suggests that the particles respond selectively to certain coherent structures in the buffer layer. Data accumulated for the wall-normal particle velocities in case A (not shown) features a less pronounced negative skewness. Unfortunately, no experimental data for the skewness of the wall-normal particle velocity pdf in channel flow could be obtained. Therefore, in order to clarify this point, more in-depth investigations of the interaction between buffer-layer structures and particles with different values of the Stokes number should be undertaken. In particular, conditional averaging of wall-normal particle motion based upon the type of the surrounding flow structures (similar to the point-particle study of Marchioli and Soldati, 2002) should provide valuable insight. Finally, we observe in figure 17(c) that the pdf of the spanwise component of the particle velocity (having a skewness near zero by virtue of symmetry) takes a shape very similar to the one found for the wall-normal component outside the buffer layer.

In order to analyze the different contributions to the Reynolds shear stress, we have computed joint probability density functions of the fluid velocity fluctuations u'_f and v'_f . The data for wall-distances of $y^+ = 20$ and 74 is shown in figures 18(a,b); an exhaustive discussion of the corresponding single-phase case can be found in Kim et al. (1987). Quadrants are defined in the usual manner, such that e.g. the second quadrant corresponds to an ejection of low-speed fluid (a positive value of v'_f coupled with negative u'_f). The joint pdfs for the present case B are found to take an elliptical shape, elongated in a direction which is slightly inclined with respect to the axis $v'_f = 0$. Therefore, the contributions from the second and the fourth quadrants dominate as in single-phase flow. It can be seen in both figures 18(a,b) that the most extreme negative fluctuations of u'_f are not significantly correlated with fluctuations v'_f of any sign, therefore not contributing to the mean Reynolds shear stress. In the logarithmic region the joint pdf tends towards a less anisotropic shape.

The fractional contributions from each quadrant to the Reynolds shear stress are given in figure 19. In the buffer layer ($y^+ = 20$) and in the logarithmic region ($y^+ = 74$) the total contribution from the second quadrant is the strongest, with the fourth quadrant closely following. The main difference with respect to the single phase data (as discussed in Kim et al., 1987) is

the relative importance of the quadrants one and three (i.e. those which correspond to positive Reynolds shear stress). In the particulate case, the fractional contributions of all four quadrants are significantly higher than in the case without particles, most probably due to fluctuations generated in the wake of particles. As discussed above, the wakes are expected to have the effect of adding additional contributions of similar magnitude to each quadrant, therefore not contributing to an increase in the average Reynolds shear stress. The plots in figure 19 also show the fractional contributions from each quadrant when applying a threshold to the magnitude of the correlation $u'_f v'_f$. At both wall-distances the contributions from the second and third quadrants become completely dominant for thresholds above five times the product of the r.m.s. intensities of u'_f and v'_f . This reflects the large value of the negative skewness of the streamwise velocity pdf, i.e. the importance of the wake structures.

The joint pdfs for the streamwise and wall-normal components of the particle velocity fluctuations at two corresponding wall-distances ($y^+ = 17$ and 73) are shown in figure 20. The overall shape of the contourlines is found to be similar to the fluid counterparts in figure 18, yet events with highly negative values of the streamwise component are absent here. The fractional contributions from each quadrant to the correlation $u'_c v'_c$ (figure omitted) agree with the respective contributions of the fluid velocity to the Reynolds shear stress. However, a faster decay of all quadrants' contribution with increasing threshold is observed for the particle velocity correlation $u'_c v'_c$, in accordance with the near-Gaussian shape of the pdf for the streamwise component (cf. figure 17a).

4 Lagrangian statistics

In order to get further insight into the particle response to fluid motion, we consider statistics which describe the evolution of the particle velocity along individual particle trajectories. The Lagrangian auto-correlation of the particle velocity components as a function of the temporal separation τ can be defined as follows (similar to Ahmed and Elghobashi, 2001):

$$R_{Lp,\alpha}(\tau) = \frac{\langle \langle u'_{c,\alpha}(t) \cdot u'_{c,\alpha}(t + \tau) \rangle_p \rangle_t}{\langle \langle (u'_{c,\alpha}(t))^2 \rangle_p \rangle_t}, \quad (7)$$

where $u'_{c,\alpha}(t) = u_{c,\alpha}(t) - \langle u_c \rangle(y_j | x_{c,2}(t) \in I_j) \delta_{\alpha 1}$ is the instantaneous velocity of the i th particle in the α direction, from which the mean streamwise particle velocity at the corresponding bin y_j has been subtracted. By way of this definition, the correlation of the fluctuating particle motion can be studied while the contribution from the mean particle drift is eliminated.

Our present results are shown in figure 21. It can be observed that all Lagrangian two-time correlation functions of case B exhibit a damped oscillation with a period of approximately $8h/u_b$ superposed upon the typical decaying curves. For case A this feature is less pronounced, but it can still be observed with a period of approximately $4h/u_b$, in particular in the wall-normal and the spanwise components. This phenomenon is believed to be related to the finite streamwise length of the computational domain. Considering that the difference between the mean velocities of the two phases is approximately equal to u_b across most of the channel width (cf. figure 10b), particles will encounter the same material fluid elements upon average after a relative turnover period of $T_{rel} = L_x/u_b$. Substituting the domain lengths of cases A and B ($L_x = 4h$ and $8h$) yields a value for T_{rel} which indeed matches the observed period separating the successive peaks of the Lagrangian two-time velocity correlation functions. However, these relative maxima of the correlation functions can only be caused by a significant interaction of particles with structures which are temporally coherent over time scales comparable to the turnover period T_{rel} . Fede, Simonin, and Villedieu (2007) have considered the problem of statistical bias caused by self-correlation of the fluid velocity along the path of heavy point-particles in homogeneous-isotropic turbulence (by means of one-way coupled simulations). They showed that choosing the parameters such that $T_{rel} \geq 4\tau_E$, where τ_E is the Eulerian integral time scale of the fluid velocity field, is sufficient in order to avoid bias of the Lagrangian correlation of the fluid velocity ‘seen’ by the

particles. With the purpose of applying this criterion to the present case, the Eulerian integral time scale can be estimated from the Eulerian integral length scale and invoking Taylor’s hypothesis. The streamwise integral length scale of the streamwise velocity component is defined as:

$$L_{f,u} = \int_0^{L_x/2} R_{uu}(x) dx, \quad (8)$$

where R_{uu} is the two-point auto-correlation function of fluid velocity. In single-phase channel flow, the data of Kim et al. (1987) yields $L_{f,u} = 0.87h$ at the centerline ($L_{f,u} = 1.2h$ at $y^+ = 21$). Supposing a convection velocity equal to the local mean velocity (Kim and Hussain, 1993), this leads to an estimate of $\tau_E = 0.74h/u_b$ at the center and $1.5h/u_b$ in the buffer layer. Therefore, based upon the single-phase data the streamwise domain size L_x in case B verifies the condition of Fede et al. (2007), while the domain in case A seems to be slightly too short in order to guarantee unbiased Lagrangian statistics. However, this a priori estimation does not seem to be able to explain that the bias effect is stronger in the case with the longer domain, where several repeated peaks up to the fifth one can be observed. Since a repeated positive correlation over four relative turnover periods requires that particles interact with fluid features of extreme longevity, the data shown in figure 21 suggests that there exist some large-scale coherent structures in the particulate flow which are not found in single-phase turbulence. In § 6 below we will indeed identify flow structures correlated over the whole box-length.

Let us return to the discussion of the Lagrangian particle velocity correlations themselves. In the absence of reference data for channel flow, we will refer to the results of Ahmed and Elghobashi (2001) obtained by DNS of homogeneous shear flow with point-particles. Their most relevant conclusions with respect to the present work are: (a) particle inertia tends to increase the Lagrangian velocity correlations; (b) mean relative velocity (caused by gravity) leads to a decrease of the correlations due to the so-called ‘crossing trajectories effect’ (Yudine, 1959); (c) the anisotropic structure of the shear flow is reflected in the particle velocity correlations.

Concerning the results shown in figure 21, we remark that for all velocity components the decay is faster in case B than in the high-inertia case A, in accordance with the results of Ahmed and Elghobashi (2001). A rough match of the curves for both cases can be obtained by rescaling the temporal separations in case A with a factor of 1.5.

We further observe from figure 21 that the streamwise (vertical) particle velocity component exhibits a much longer decorrelation time than the two cross-stream (horizontal) components, with a first zero-crossing occurring after as much as 85 (45) bulk time units in case A (B). The anisotropy is also evidenced by the integral time scales computed from the Lagrangian correlation functions, viz.

$$T_{Lp,\alpha} = \int_0^\infty R_{Lp,\alpha}(\tau) d\tau, \quad (9)$$

which are shown in table 5. It is well-known that the time scales of fluid structures in channel flow are strongly anisotropic. Choi, Yeo, and Lee (2004) have computed Lagrangian velocity correlations of fluid elements in the absence of particles. Their data at the center of the channel suggests a ratio of decorrelation time scales of roughly 1 : 0.4 : 0.5 for the three fluid velocity components $u_f : v_f : w_f$. By comparison, the corresponding correlations for the particle velocity in the present cases exhibit a much higher anisotropy of the streamwise component. This difference is believed to be related to the modified flow structure in the particulate case, where we have already observed a strongly enhanced intensity of the streamwise velocity fluctuations (cf. figure 11). Unfortunately, no Lagrangian correlation data for fluid elements is available for the present cases. However, we will provide evidence of increased Eulerian two-point fluid velocity correlations in § 6 below.

Concerning the crossing trajectories effect, the usual measure for gauging its importance is the ratio between the relative mean velocity and the r.m.s. fluid velocity fluctuations in the mean slip direction, viz. $|\langle u_c \rangle - \langle u_f \rangle| / \sqrt{\langle u'_f u'_f \rangle}$ (Csanady, 1963). From figures 10(b) and 11(a) we deduce that the ratio for both cases ranges between 4 and 5 across most of the channel width. The

relative motion can therefore be judged as sufficiently strong for the particles to experience the consequences of their continuous change of the surrounding fluid environment, which is expected to contribute to a reduction of the temporal auto-correlation of particle velocities. However, in order to isolate the impact of the crossing trajectories effect upon the correlation functions, results from cases with different drift velocities and otherwise identical parameters would be necessary.

The definition of the Lagrangian velocity correlation discussed so far does not distinguish the particles according to their location along the inhomogeneous direction. This distinction can be accomplished by modifying relation (7) such that the sums are performed only over those particles which are located within a wall-normal interval I_j at the initial time t . In doing so, one obtains correlation functions which turn out to have a similar shape to the globally averaged functions shown in figure 21, but where the decay depends upon the particle's initial wall-distance. Figure 22 shows the dependency between the integral time scale and the initial particle coordinate y in case B. The Lagrangian integral time scales associated with the streamwise and wall-normal particle velocity can be seen to increase progressively with the wall-distance; the spanwise component exhibits a similar behavior up to $\bar{y} \approx 0.8$, then it decreases again towards the center of the channel. The trend of faster decorrelation near the wall is consistent with the fact that the length scales of the dominant turbulent structures in channel flow increase with the wall-distance. Choi et al. (2004) have shown for single-phase flow that this spatial inhomogeneity leads to a faster decay of the velocity correlations of fluid elements when they are released from smaller wall-distances. It is believed that a similar reasoning applies to our solid particles, with smaller fluid scales near the wall leading to a faster decorrelation of the particle velocity in that region.

5 Spatial structure of the dispersed phase

In this section we are concerned with the possible formation of instantaneous particle agglomerations in the flow. As discussed in the introduction, at least two mechanisms for clustering appear to be available: interaction with turbulent flow structures (i.e. 'preferential concentration') and the particle-wake effect. In order to determine whether agglomerations play a significant role, an analysis of inter-particle distances and local number densities is required. For this purpose we have applied four different diagnostic methods to our data: the average distance to the nearest neighbor, cluster detection, the probability of local particle concentration and the particle-pair correlation function.

Let us define the average distance to the nearest particle as follows:

$$d_{min} = \frac{1}{N_p} \sum_{i=1}^{N_p} \min_{\substack{j=1 \\ j \neq i}}^{N_p} (d_{i,j}), \quad (10)$$

where $d_{i,j} = |\mathbf{x}_c^{(i)} - \mathbf{x}_c^{(j)}|$ is the distance between the centers of particles i and j . The time evolution of the quantity d_{min} , normalized by its value for a homogeneous distribution with the same solid volume fraction, $d_{min}^{hom} = (|\Omega|/N_p)^{1/3}$, has been plotted in figure 23. Here the ratio d_{min}/d_{min}^{hom} has a lower bound of 0.2 (corresponding to each particle being in contact with at least one other particle) and an upper bound of unity (homogeneous distribution). Actual values recorded during our simulations vary mildly between 0.5 and 0.6, which is in fact very close to the value of a random distribution (numerically determined as 0.5621). It is interesting to note that direct simulations of pure sedimentation in triply periodic domains also yield values for the mean minimum inter-particle distance which (when normalized with d_{min}^{hom}) fluctuate around 0.55 (Kajishima, 2004).

An alternative way of characterizing the spatial structure of the dispersed phase is by searching directly for the presence of particle clusters. Here we define a cluster as a set of particles of which each member is within a distance l_c of at least one other member (Wylie and Koch, 2000). Since cluster detection is a computationally expensive task, it is necessary to resort to a fast numerical algorithm. We have implemented the technique suggested by Melheim (2005) which was applied to 400 (50) instantaneous particle distributions of case A (B), from which the probability of

the occurrence of clusters with different numbers of members n_c was determined for each case. Figure 24(a, b) shows our results for two different cut-off lengths $l_c = 2.5D$ and $4D$. It can be observed that the pdf for the occurrence of clusters is a rapidly decaying function of the number of its members, and that the curve flattens as expected when increasing the cut-off length. Both DNS cases yield fairly similar results. The plots also include the corresponding pdf for a random particle distribution with the same solid volume fraction (numerically determined from 100 realizations), which is found to collapse with the DNS data.

Since particles can interact over long distances via their wakes, the cluster definition was then modified in order to take the non-isotropic structure of the wakes into account. Instead of using a spherical cut-off radius, we define clusters through an ellipsoidal definition. More specifically, two particles i and j are considered as members of a cluster if their positions obey

$$\sum_{\alpha=1}^3 \frac{(x_{c,\alpha}^{(i)} - x_{c,\alpha}^{(j)})^2}{l_{c,\alpha}^2} \leq 1, \quad (11)$$

for a given cut-off axis vector with components $l_{c,\alpha}$. Figure 24(c) shows the pdf of the occurrence of clusters using a streamwise-elongated elliptical definition with a 3 : 1 : 1 axis ratio. It is found that the probability for large clusters indeed increases with respect to a spherical definition with the radius corresponding to the minor axis length. However, the random particle distribution again exhibits the same pdf as the DNS data to within statistical uncertainty.

Several authors have used the statistics of local particle concentration as a measure of the tendency for preferential concentration (Squires and Eaton, 1991; Wang and Maxey, 1993; Fessler, Kulick, and Eaton, 1994; Aliseda, Cartellier, Hainaux, and Lasheras, 2002). The concentration is determined by subdividing the flow domain into smaller boxes (with linear dimensions H_x, H_y, H_z), counting the number of particles in each box, $n_{p,box}$, and then dividing by the box volume, i.e. $C = n_{p,box}/(H_x H_y H_z)$. This process is repeated for each field, and finally statistics are computed over the homogeneous directions and the number of snapshots. In the present case, the width of all boxes in the wall-normal direction is taken as one particle diameter ($H_y = D$), therefore allowing for a distinction of the results with respect to the wall-distance; the box-size in the two wall-parallel directions was varied between $H_x = H_z = 5D$ and $40D$. Figure 25(a) shows the pdf of the local particle concentration in case B at a wall-distance of $y^+ = 28$ for a cross-stream (horizontal) box-dimension of $H_x = H_z = 20D$. The concentration C is normalized by the average concentration at the same wall-distance, C_0 . It can be seen that the DNS data agrees very well with a Poisson distribution which characterizes the probability of a random process (Squires and Eaton, 1991). The difference between the pdf from the DNS data and the Poisson distribution can be quantified by summing the square of the difference between both probabilities (Wang and Maxey, 1993), viz.

$$D_2 = \sum_{n=1}^{N_p} (P(n) - P_{Poisson}(n))^2, \quad (12)$$

where $P(n)$ is the probability of finding n particles in a given box. The quantity D_2 is shown in figure 25(b) as a function of the linear box-dimension and for different wall-distances. We observe that the difference always remains below 10^{-3} . Again, this definition can be extended to the non-isotropic case by defining elongated boxes (i.e. $H_x > H_z$). The results (which are not shown here) lead to the same conclusion: the local concentration closely follows a Poisson distribution.

As an additional measure of the spatial structure of the dispersed phase, we have determined the pairwise particle distribution function. This quantity corresponds to the probability of finding a second particle at a certain distance from a given particle. In order to investigate the two homogeneous directions separately, we have defined a directional (as opposed to radial) distribution function for streamwise and spanwise separations. In both directions, the curves are found to be essentially constants (the figures are omitted), indicating that all possible inter-particle distances are roughly of equal probability, irrespective of the wall-distance.

Finally we can conclude from the different diagnostic techniques employed here that the instantaneous spatial distribution of particles in the present cases is not significantly different from the distribution generated by a random process. This point will be further discussed in § 7.

6 Coherent flow structures

We have come across indications of a significantly modified turbulence structure with respect to single-phase channel flow at several points in the previous discussion. Here we attempt to identify the coherent flow structures which are responsible for the observed differences in the various statistical quantities.

Figure 26 shows isosurfaces of the fluctuations of the streamwise velocity component for an instantaneous flow field in case B. The isovalues ($u' = \pm 3.6u_\tau$) are chosen such that in the corresponding single-phase flow almost exclusively buffer-layer streaks are visualized. In the present case, however, the picture is fundamentally different. First, we recognize in figure 26(*b, d*) the wakes trailing individual particles as streamwise elongated surfaces with negative fluctuation values (due to fluid upflow and negative particle buoyancy). These wakes can be distinguished more clearly in figure 27 where a zoom into the graphs of figure 26(*b, d*) is provided. At the present particle Reynolds number, particle wakes have a characteristic streamwise extension of less than one channel half width and a cross-stream extension comparable to the particle diameter. In addition, we observe in figure 26 very large coherent structures with streamwise dimensions of the order of the length of the current domain ($8h$) and cross-stream scales comparable to the channel half-width. Very large structures with both signs of the isovalue for u' are found, the negative-valued structures being more difficult to discern due to the cluttering of the image by the large number of particle wakes. Visualizations of successive snapshots reveal that these flow structures evolve on a relatively large time scale. An example of such a temporal sequence is shown in figure 28, where we can identify structures over an interval of approximately 45 bulk time units while they slowly revolve around each other in the cross-stream plane. This temporal coherence of the large-scale structures is at the origin of the slow convergence of the Eulerian statistics in the present case. The lack of symmetry of the streamwise momentum balance with respect to the midplane (observed in § 3.1, figure 5*a, b* as well as figure 33*a* of appendix A) is due to the marginal sampling of these large scales over the present observation interval. Furthermore, the presence of flow structures with a lifetime of tens of bulk time units explains the repeated peaks of the Lagrangian particle velocity auto-correlation function discussed in § 4 (cf. figure 21). Finally, it should be remarked that both particle wakes and the very large structures contribute to the strong increase in the streamwise r.m.s. fluid velocity, leading to the overall turbulence enhancement (cf. figure 11).

In order to investigate whether the particles respond to the large-scale perturbations of the streamwise fluid velocity, we have visualized the instantaneous particle motion. The particles have been classified according to their streamwise velocity fluctuation: those with a high positive fluctuation value ($u'_c \geq 0.2u_b$), highly negative fluctuation ($u'_c \leq -0.2u_b$) and small fluctuation ($-0.2u_b < u'_c < 0.2u_b$). The instantaneous locations of the three classes of particles are shown in figures 29 and 30 at the same time as the flow field in figure 26. The high-speed particles of both signs are clearly found in regions with a streamwise elongated shape, whereas the particles with streamwise velocity fluctuation amplitudes below the threshold are more or less equally distributed everywhere else. Comparing the particle distribution with the locations of the fluid structures (figure 29 versus 26), a strong spatial correlation between high-intensity velocity fluctuations of the two phases is indeed observed. It has been confirmed by visualizing time-series that the spatial distribution of particles with intense streamwise velocity fluctuations exhibits the same high temporal coherence as the fluid counterpart. In particular, animations show that the large-scale organization of the flow starts to be visible approximately 12 bulk time units after introducing the particles into the flow. Subsequently, it remains a prominent feature over the entire observation interval.

In order to further confirm the statistical significance of the observed instantaneous flow structures we have computed Eulerian two-point correlations of fluid velocity (taking into account only

points in the actual fluid domain) from 12 instantaneous flow fields. The data for case B is shown in figure 31 (for streamwise separations) and figure 32 (spanwise separations). For all components and in both spatial directions the decay at small separations is found to be enhanced in the present case as compared to the single-phase reference data. This result reflects the presence of smaller scales in the vicinity of the particles' surfaces as well as in their wakes. For larger separations the correlation functions of the particulate case and the single-phase flow cross over. The most pronounced features are the finite correlation values of the streamwise velocity component for the largest separations. These correlation values are positive (negative) for large streamwise (spanwise) separations. This result is fully consistent with the presence of the observed large-scale structures. As a further consequence of the modified flow structure, all streamwise correlation amplitudes increase with the wall-distance contrary to what is found in single phase flow (figure 31). It is also remarkable here that for intermediate spanwise separations in the range of $50 \leq r_z^+ \leq 200$ the correlation functions for the streamwise and spanwise velocity components do not exhibit the characteristic negative minimum which is directly linked to the average spacing of low- and high-speed buffer-layer streaks (Kim et al., 1987). We still observe a weaker local minimum of the wall-normal component at the smallest wall-distance (figure 32b). The evidence from the fluid velocity correlation functions shows that the structures which we have observed instantaneously have a large significance for the flow statistics, masking in part even the signatures of the usual near-wall turbulence structures.

The equivalent to the Eulerian two-point velocity correlation for the dispersed phase is the so-called particle pair velocity correlation (cf. Reeks, Fabbro, and Soldati, 2006). It was confirmed that the spatial decay of the particle pair velocity correlations (figures omitted) exhibits the same characteristic features as the counterparts for the fluid velocity. Thereby we have statistically substantiated the correspondence between particle motion and large-scale fluid structures observed in instantaneous flow fields.

7 Summary and discussion

We have conducted a DNS study of turbulent particulate channel flow in a doubly-periodic domain, considering finite-size rigid particles with numerically resolved phase interfaces. The simulations were performed in the dilute regime, allowing for an approximate treatment of direct particle encounters. In our simulations we have considered spherically-shaped heavy particles whose buoyancy was adjusted such that the terminal velocity matches the bulk flow velocity. The fluid was driven upwards by a mean pressure gradient, thereby fluidizing particles in the center of the channel while particles near the walls moved downwards upon average. For the present bulk Reynolds number of 2700 and particle diameter of $1/20$ of the channel half-width (corresponding to approximately 11 wall units), this leads to a terminal particle Reynolds number of 136. Two different density ratios were considered, differing by a factor of 4.5. The corresponding Stokes numbers of the two types of particles were $\mathcal{O}(10)$ in the near-wall region and $\mathcal{O}(1)$ in the outer flow. The case with lower particle inertia was run in a computational domain with a length of 8 and 4 channel half-widths in the two wall-parallel directions, involving 4096 particles and integration times of $\mathcal{O}(100)$ bulk flow time units.

We have presented statistical data for the Eulerian one-point moments of the velocities of both phases, velocity probability density functions, Lagrangian particle velocity correlations, various measures for the spatial structure of the dispersed phase, flow visualizations and Eulerian two-point correlations. The main results can be summarized as follows.

1. The presence of particles strongly affects the carrier flow. On the one hand the mean flow profile tends towards a concave shape due to the interplay between the modified Reynolds shear stress profile and the mean force exerted by the particles upon the fluid. The latter contribution is directly linked to the non-homogeneity of the mean solid volume fraction which has the effect of bringing more streamwise momentum towards the wall. On the other hand the intensity of turbulence is strongly enhanced with respect to the single-phase flow at the same bulk Reynolds number. This enhancement is mostly due to an increase in the

streamwise velocity fluctuations, whereby the anisotropy of the Reynolds stress tensor is considerably modified.

2. At the chosen parameter values there is no significant clustering of particles. By ‘clustering’ we understand deviations from the local mean solid volume fraction beyond the extent that can be expected from a random process.
3. The two dominating flow features are particle wakes and very large jet-like structures. The wakes constitute regions with low streamwise velocity (due to mean upflow and negative particle buoyancy), causing a marked negative skewness of the corresponding pdf. The large-scale structures appear as regions with positive or negative streamwise velocity fluctuations extending over eight channel half widths (the entire domain length) in the streamwise direction and approximately one half width in the cross-stream directions. As a consequence, the Eulerian two-point correlation of the streamwise fluid velocity exhibits finite values at large streamwise and spanwise separations. Furthermore, it was observed that the particle motion is strongly affected by these large-scale flow structures, whose signatures were found in Lagrangian particle velocity correlations and Eulerian particle pair velocity correlations.
4. The differences between the two flow cases were relatively small. The fact that the high-inertia case was computed in a smaller computational domain might account partly for the observed differences. An exception are the Lagrangian particle velocity correlations which clearly exhibit longer decorrelation times in the high-inertia case.

The fact that no particle agglomerations were found while the formation of new large-scale flow structures was detected merits further discussion. With respect to particle agglomerations it must be concluded that the two known mechanisms for their formation are not effective in the present context. For the preferential accumulation effect to generate significant segregation of particles by centrifugal ejection from vortical structures, the particles need to be small compared to the dominant (i.e. high vorticity) flow structures. The particles studied here are probably too large in order to accumulate outside of the high-vorticity regions. This is particularly true in the near-wall region, where the present particles’ size is comparable to the typical cross-stream dimensions of the streamwise vortices.

Concerning the wake attraction effect, i.e. the formation of clusters due to the decreased drag experienced by trailing particles, it can be inferred from our results that the particle Reynolds number in the present study is probably too low for this mechanism to be of importance. In the pure sedimentation case (Kajishima, 2004) particle clusters start to appear at a particle Reynolds number of 200; in the case with grid-generated turbulent background flow (Nishino and Matsushita, 2004) trains of particles were found for particle Reynolds numbers of 140. It should be noted that in both of those studies the suspension was even more dilute than here. In turbulent channel flow wake-induced clusters have to our knowledge not been reported in the literature. Therefore, it would be interesting to perform future simulations with higher slip velocities in order to establish whether the wake-attraction mechanism is able to actuate in channel flow and to determine a critical Reynolds number.

Even in the absence of particle agglomerations (i.e. significant perturbations of the solid volume fraction) the flow is found to exhibit large-scale organization in the form of streak-like velocity perturbations. It should be emphasized that this feature is clearly particle-induced since no corresponding flow structures exist in single-phase channel flow. Since these large-scale flow structures were found to have a substantial effect on various statistical quantities (two-point velocity correlations, Lagrangian particle velocity correlations, r.m.s. fluid velocity fluctuations) the question about their origin is of great interest. It is plausible to believe that a mechanism related to hydrodynamic instability is responsible for the formation of the large-scale flow structures. In this scenario it can be imagined that the addition of particles to the turbulent channel flow triggers an intrinsic instability eventually leading to the observed velocity perturbations. However, at the present time there is no confirmation of the existence of such an instability mechanism. In this context it should be remarked that Matas, Morris, and Guazzelli (2003) found a decrease of the critical

Reynolds number when adding neutrally-buoyant particles above a certain size ($D \geq d_{pipe}/65$) to laminar pipe flow. These authors speculated that the lowered transition threshold is due to the particle-induced velocity fluctuations triggering subcritical transition. The influence of the presence of dispersed particles upon the stability characteristics of pipe or channel flow deserves further investigation in the future.

One further question which naturally arises in relation with the emergence of flow scales of the order of the streamwise period of the computational domain is whether the finite box size might play a decisive role. In particular, the typical streamwise size of these structures cannot be precisely determined if no decorrelation within the fundamental period takes place. It should be mentioned that these largest scales are not clearly observed in the case with the smaller domain (case A). On the other hand, computing the flow in much larger domains than the one used in case B is a challenging task, since those simulations are already on the limit of what can be afforded with the present algorithm on the largest available hardware. Nevertheless, we have recently initiated a companion simulation with twice the streamwise period of case B and otherwise identical conditions, corresponding to a Eulerian grid with more than $2.6 \cdot 10^9$ nodes. The results of this extended simulation—when available—will hopefully shed light on the scaling of the large structures.

Acknowledgments

The author is grateful to A. Pinelli for helpful comments contributing to the improvement of an earlier version of this manuscript. This work was supported by the Spanish Ministry of Education and Science under the ‘Ramón y Cajal’ program (contract DPI-2002-040550-C07-04) and through grant ENE2005-09190-C04-04/CON. The computer resources, technical expertise and assistance provided by the Barcelona Supercomputing Center - Centro Nacional de Supercomputación are thankfully acknowledged.

A The effect of evaluating Eulerian statistics over the composite flow field

In order to assess the effect of computing the Eulerian one-point statistics of the carrier phase over the composite flow field (including solid and fluid nodes), we have applied this procedure to 12 instantaneous flow fields of case B which were taken over an interval of approximately 55 bulk time units. For the purpose of comparison, we have computed the corresponding quantities by averaging only over nodes which are located in the fluid domain, using the same set of flow fields. This ‘fluid-only’ average shall be denoted by $\langle \cdot \rangle_f$. Both results are compared in figure 33. It can be seen that a significant difference is only obtained for the streamwise normal stress component, whereas the other stress components as well the mean velocity are not noticeably affected. The maximum normalized difference between the results of the two methods, as defined by

$$\mathcal{E}(\langle u \rangle) = \frac{\max_y |\langle u \rangle_f - \langle u \rangle|}{\max_y \langle u \rangle_f}, \quad (13)$$

(and similarly for the other quantities) is given in table 6. It can be seen that the difference has a maximum of 6.7% in the case of the streamwise velocity fluctuation, while it is significantly smaller for all other quantities. In particular, the difference for the mean velocity is below 0.7%. The larger difference for the quantities related to the streamwise velocity components is due to the fact that the virtual fluid velocity inside the heavy particles in upward flow represents principally a low-velocity perturbation with respect to the streamwise velocity of the surrounding fluid. Therefore, averaging over the composite flow field yields an underestimation of the mean velocity and an overestimation of the r.m.s. value of the streamwise velocity fluctuations. Figure 34 shows the difference between the two methods of computing these two moments of the streamwise velocity, plotted as a function of the wall-normal coordinate. It can be seen that the difference is directly

proportional to the local solid volume fraction (computed from the corresponding 12 particle fields) with a coefficient of $\mathcal{O}(1)$. In particular, the least-squares fit of the data yields:

$$(\langle u \rangle_f - \langle u \rangle)/u_b \approx -1.4682 \langle \phi_s \rangle \quad (14a)$$

$$(\langle u'u' \rangle_f - \langle u'u' \rangle)/u_b^2 \approx 1.3634 \langle \phi_s \rangle, \quad (14b)$$

with standard deviations of $\sigma_u = 2.1966 \cdot 10^{-4}$ and $\sigma_{uu} = 2.7847 \cdot 10^{-4}$, respectively.

The result of the preceding paragraph is consistent with the following estimation. Let us assume that particles maintain a velocity equal to their terminal settling velocity with respect to the surrounding fluid velocity at all times and particle rotation can be neglected, i.e. the streamwise component of the virtual fluid velocity inside the solid regions can be expressed as $u(\mathbf{x} \in \mathcal{S}) \approx \langle u \rangle_f - |u_{c,\infty}|$; fluctuations of the solid volume fraction are also neglected. Then it can be shown that for the mean velocity: $\langle u \rangle - \langle u \rangle_f = -|u_{c,\infty}| \langle \phi_s \rangle$. Likewise, for the streamwise component of the stress tensor: $\langle u'u' \rangle - \langle u'u' \rangle_f = -\langle u'u' \rangle_f \langle \phi_s \rangle + |u_{c,\infty}|^2 (\langle \phi_s \rangle - \langle \phi_s \rangle^2)$; since we have imposed $|u_{c,\infty}| = u_b$ (and the following two relations hold: $\langle \phi_s \rangle \ll 1$ and $\langle u'u' \rangle_f \ll u_b$), the dominant term is $|u_{c,\infty}|^2 \langle \phi_s \rangle$. This suggests that for both quantities the difference scales with the local solid volume fraction, as was indeed observed in figure 34.

From this comparison we can conclude that the statistics accumulated at run-time of the simulation, while not distinguishing between fluid and solid locations, overestimate the r.m.s. value of the streamwise velocity fluctuations by up to 6.7%, while affecting the other fluctuating components much less and to an even lesser extent the mean velocity. The excellent fit of the present data with a linear function of the mean solid volume fraction enables us to correct the statistics of $\langle u'u' \rangle$ which were accumulated at run-time.

B The mean streamwise momentum balance

Since the driving pressure gradient is not fixed in our simulations, we need to determine it first. For this purpose we consider the streamwise component of the momentum equation,

$$\partial_t \mathbf{u} + (\mathbf{u} \cdot \nabla) \mathbf{u} + \nabla p = \nu \nabla^2 \mathbf{u} + \mathbf{f} \quad (15)$$

where \mathbf{u} is the vector of fluid velocities, p the pressure normalized with the fluid density (ρ_f), ν the kinematic viscosity and \mathbf{f} the volume force term which serves to impose the rigid body motion upon the fluid at the location of the particles. Integrating (15) over the whole spatial domain Ω and a sufficiently long temporal interval T to allow for a statistically steady state where the velocity field only depends upon the wall-normal coordinate, viz.

$$\frac{\partial \langle p \rangle}{\partial x} 2h + 2u_\tau^2 = \frac{1}{TL_x L_z} \int_{t_0}^{t_0+T} \int_{\Omega} f_x \, d\mathbf{x} \, dt = \frac{1}{TL_x L_z} \int_{t_0}^{t_0+T} \sum_{i=1}^{N_p} \int_{x \in \mathcal{S}^{(i)}} f_x \, d\mathbf{x} \, dt, \quad (16)$$

where the last integral extends over the subvolume $\mathcal{S}^{(i)}$ occupied by the i th particle. The force integral can be eliminated by making use of the Newton equation for the linear particle motion (Uhlmann, 2005a, equ. 13), which states:

$$V_c \left(\frac{\rho_p}{\rho_f} - 1 \right) \dot{\mathbf{u}}_c^{(m)} = - \int_{x \in \mathcal{S}^{(i)}} \mathbf{f} \, d\mathbf{x} + \left(\frac{\rho_p}{\rho_f} - 1 \right) V_c \mathbf{g}, \quad (17)$$

where $\mathbf{u}_c^{(m)}$ is the vector of the m th particle's translational velocity. Substituting the streamwise component of (17) into (16) and making use of the fact that the flow is statistically stationary (i.e. the average particle acceleration vanishes) yields the mean streamwise pressure gradient:

$$\frac{\partial \langle p \rangle}{\partial x} = -\frac{u_\tau^2}{h} + \Phi_s \left(\frac{\rho_p}{\rho_f} - 1 \right) g_x. \quad (18)$$

In order to derive the y -dependent streamwise momentum balance, we now integrate equation (15) over wall-parallel planes and time:

$$\frac{d\langle u'v' \rangle}{dy} - \frac{u_\tau^2}{h} + \Phi_s \left(\frac{\rho_p}{\rho_f} - 1 \right) g_x = \nu \frac{d^2 \langle u \rangle}{dy^2} + \langle f_x \rangle, \quad (19)$$

where the Reynolds decomposition $\mathbf{u} = (\langle u \rangle, 0, 0) + \mathbf{u}'$ has been substituted. Equation (19) could be used for evaluating the convergence of the statistics. However, the local average force density $\langle f_x \rangle$ at the Eulerian grid nodes is not directly available in our data-sets. Alternatively, the quantity $\langle f_x \rangle$ can be expressed by averaging the equation for the linear particle acceleration (17) over finite wall-normal bins, similar to the operation defined in (4). This procedure amounts to associating the sum of the forces applied to each particle with the particle's center location, i.e. the force density is computed as follows:

$$\langle f_x \rangle(y_j) \approx \frac{1}{n_{obs} L_x L_z |I_{y_j}|} \sum_{l=1}^{n_{obs}} \sum_{i=1}^{N_p} \int_{x \in \mathcal{S}^{(i)}} f_x(t_l) d\mathbf{x}. \quad (20)$$

$y_c^{(i)}(t_l) \in I_{y_j}$

The same operator applied to the equation of particle acceleration (17), assuming statistical stationarity, yields:

$$\langle f_x \rangle(y_j) = \left(\frac{\rho_p}{\rho_f} - 1 \right) g_x \langle \phi_s \rangle(y_j). \quad (21)$$

Figure 35 shows that the equality (21) is indeed verified across the entire channel by the data accumulated during our simulations. Finally, we substitute (21) into (19) to obtain the desired streamwise momentum balance equation (5) given in the main text (cf. § 3.1).

References

- A.M. Ahmed and S. Elghobashi. On the mechanisms of modifying the structure of turbulent homogeneous shear flows by dispersed particles. *Phys. Fluids*, 12(11):2906–2930, 2000.
- A.M. Ahmed and S. Elghobashi. Direct numerical simulation of particle dispersion in homogeneous turbulent shear flows. *Phys. Fluids*, 13(11):3346–3364, 2001.
- A. Aliseda, A. Cartellier, F. Hainaux, and J.C. Lasheras. Effect of preferential concentration on the settling velocity of heavy particles in homogeneous isotropic turbulence. *J. Fluid Mech.*, 468:77–105, 2002.
- P. Bagchi and S. Balachandar. Effect of turbulence on the drag and lift of a particle. *Phys. Fluids*, 15(11):3496–3513, 2003.
- P. Bagchi and S. Balachandar. Response of the wake of an isolated particle to an isotropic turbulent flow. *J. Fluid Mech.*, 518:95–123, 2004.
- T.M. Burton and J.K. Eaton. Fully resolved simulations of particle-turbulence interaction. *J. Fluid Mech.*, 545:67–111, 2005.
- M. Caporaloni, F. Tampieri, F. Trombetti, and O. Vittori. Transfer of particles in nonisotropic air turbulence. *J. Atmosph. Sci.*, 32:565–568, 1975.
- J.-I. Choi, K. Yeo, and C. Lee. Lagrangian statistics in turbulent channel flow. *Phys. Fluids*, 16(3):779–793, 2004.
- R. Clift, J.R. Grace, and M.E. Weber. *Bubbles, drops and particles*. Academic Press, 1978.
- G.T. Csanady. Turbulent diffusion of heavy particles in the atmosphere. *J. Atmosph. Sci.*, 20:201–208, 1963.

- E.-J. Ding and C.K. Aidun. The dynamics and scaling law for particles suspended in shear flow with inertia. *J. Fluid Mech.*, 423:317–344, 2000.
- J.K. Eaton and J.R. Fessler. Preferential concentration of particles by turbulence. *Int. J. Multiphase Flow*, 20(Suppl.):169–209, 1994.
- E.A. Fadlun, R. Verzicco, P. Orlandi, and J. Mohd-Yusof. Combined immersed-boundary finite-difference methods for three-dimensional complex flow simulations. *J. Comput. Phys.*, 161:35–60, 2000.
- P. Fede, O. Simonin, and P. Villedieu. Crossing trajectory effect on the subgrid turbulence seen by solid inertial particles. In M. Sommerfeld, editor, *ICMF 2007*, Proc. 6th Int. Conf. Multiphase Flow, Leipzig, Germany, 2007.
- A. Ferrante and S. Elghobashi. On the physical mechanisms of two-way coupling in particle-laden isotropic turbulence. *Phy. Fluids*, 15(2):315–329, 2003.
- J.R. Fessler, J.D. Kulick, and J.K. Eaton. Preferential concentration of heavy particles in a turbulent channel flow. *Phys. Fluids*, 6(11):3742–3749, 1994.
- A.F. Fortes, D.D. Joseph, and T.S. Lundgren. Nonlinear mechanics of fluidization of beds of spherical particles. *J. Fluid Mech.*, 177:467–483, 1987.
- R. Glowinski, T.-W. Pan, T.I. Hesla, and D.D. Joseph. A distributed Lagrange multiplier/fictitious domain method for particulate flows. *Int. J. Multiphase Flow*, 25:755–794, 1999.
- R. Glowinski, T.W. Pan, T.I. Hesla, D.D. Joseph, and J. Périaux. A fictitious domain approach to the direct numerical simulation of incompressible viscous flow past moving rigid bodies: Application to particulate flow. *J. Comput. Phys.*, 169:363–426, 2001.
- K. Hadinoto, E.N. Jones, C. Yurteri, and J.S. Curtis. Reynolds number dependence of gas-phase turbulence in gas-particle flows. *Int. J. Multiphase Flow*, 31:416–434, 2005.
- G. Hetsroni. Particles-turbulence interaction. *Int. J. Multiphase Flow*, 15(5):735–746, 1989.
- K. Höfler and S. Schwarzer. Navier-Stokes simulation with constraint forces: Finite-difference method for particle-laden flows and complex geometries. *Phys. Rev. E*, 61(6):7146–7160, 2000.
- T. Kajishima. Numerical investigation of collective behaviour of gravitationally settling particles in a homogeneous field. In Y. Matsumoto, K. Hishida, A. Tomiyama, K. Mishima, and S. Hosokawa, editors, *Proc. ICMF 2004 (5th Int. Conf. Multiphase Flow)*, Yokohama, 2004.
- T. Kajishima and S. Takiguchi. Interaction between particle clusters and particle-induced turbulence. *Int. J. Heat Fluid Flow*, 23:639–646, 2002.
- T. Kajishima, S. Takiguchi, H. Hamasaki, and Y. Miyake. Turbulence structure of particle-laden flow in a vertical plane channel due to vortex shedding. *JSME Int. J., Series B*, 44(4):526–535, 2001.
- K.T. Kiger and C. Pan. Suspension and turbulence modification effects of solid particulates on a horizontal turbulent channel flow. *J. Turbulence*, 3(19):1–17, 2002.
- I. Kim, S. Elghobashi, and W.A. Sirignano. Three-dimensional flow over two spheres placed side by side. *J. Fluid Mech.*, 246:465–488, 1993.
- I. Kim, S. Elghobashi, and W.A. Sirignano. On the equation for spherical-particle motion: effect of Reynolds and acceleration numbers. *J. Fluid Mech.*, 367:221–253, 1998.
- J. Kim and F. Hussain. Propagation velocity of perturbations in turbulent channel flow. *Phys. Fluids A*, 5(3):695–706, 1993.

- J. Kim, P. Moin, and R. Moser. Turbulence statistics in a fully developed channel flow at low Reynolds number. *J. Fluid Mech.*, 177:133–166, 1987.
- J.D. Kulick, J.R. Fessler, and J.K. Eaton. Particle response and turbulence modification in fully developed channel flow. *J. Fluid Mech.*, 277:109–134, 1994.
- C. Marchioli and A. Soldati. Mechanisms for particle transfer and segregation in a turbulent boundary layer. *J. Fluid Mech.*, 468:283–315, 2002.
- J.-P. Matas, J.F. Morris, and E. Guazzelli. Transition to turbulence in particulate pipe flow. *Phys. Rev. Lett.*, 90(1):014501, 2003.
- M.R. Maxey. The gravitational settling of aerosol particles in homogeneous turbulence and random flow fields. *J. Fluid Mech.*, 174:441–465, 1987.
- J.A. Melheim. Cluster integration method in Lagrangian particle dynamics. *Comput. Phys. Commun.*, 171(3):155–161, 2005.
- R.D. Moser, J. Kim, and N.N. Mansour. Direct numerical simulation of turbulent channel flow up to $Re_\tau = 590$. *Phys. Fluids*, 11(4):943–945, 1999.
- K. Nishino and H. Matsushita. Columnar particle accumulation in homogeneous turbulence. In Y. Matsumoto, K. Hishida, A. Tomiyama, K. Mishima, and S. Hosokawa, editors, *Proc. ICMF 2004 (5th Int. Conf. Multiphase Flow)*, Yokohama, Japan, 2004.
- T.W. Pan, D.D. Joseph, R. Bai, R. Glowinski, and V. Sarin. Fluidization of 1204 spheres: simulation and experiment. *J. Fluid Mech.*, 451:169–191, 2002.
- Y. Pan and S. Banerjee. Numerical simulation of particle interactions with wall turbulence. *Phys. Fluids*, 8(10):2733–2755, 1996.
- Y. Pan and S. Banerjee. Numerical investigation of the effects of large particles on wall-turbulence. *Phys. Fluids*, 9(12):3786–3807, 1997.
- R.N. Parthasarathy and G.M. Faeth. Turbulence modulation in homogeneous dilute particle-laden flows. *J. Fluid Mech.*, 220:485–514, 1990.
- C.S. Peskin. The immersed boundary method. *Acta Numerica*, 11:479–517, 2002.
- C.S. Peskin. *Flow patterns around heart valves: A digital computer method for solving the equations of motion*. PhD thesis, Albert Einstein College of Medicine, 1972.
- M.W. Reeks. The transport of discrete particles in inhomogeneous turbulence. *J. Aerosol Sci.*, 14(6):729–739, 1983.
- M.W. Reeks, L. Fabbro, and A. Soldati. In search of random uncorrelated particle motion (RUM) in a simple random flow field. In *Proceedings of FEDSM 2006*, number FEDSM2006-98383, 2006.
- C.B. Rogers and J.K. Eaton. The behavior of solid particles in a vertical turbulent boundary layer. *Int. J. Multiphase Flow*, 16(5):819–834, 1990.
- D.W. Rouison and J.K. Eaton. On the preferential concentration of solid particles in turbulent channel flow. *J. Fluid Mech.*, 428:149–169, 2001.
- Y. Sato, U. Fukuichi, and K. Hichida. Effect of inter-particle spacing on turbulence modulation by Lagrangian PIV. *Int. J. Heat Fluid Flow*, 21:554–561, 2000.
- K.D. Squires and J.K. Eaton. Particle response and turbulence modification in isotropic turbulence. *Phys. Fluids A*, 2(7):1191–1203, 1990.

- K.D. Squires and J.K. Eaton. Preferential concentration of particles by turbulence. *Phys. Fluids A*, 3(5):1169–1178, 1991.
- S. Sundaram and L.R. Collins. A numerical study of the modulation of isotropic turbulence by suspended particles. *J. Fluid Mech.*, 379:105–143, 1999.
- Y. Suzuki, M. Ikenoya, and N. Kasagi. Simultaneous measurement of fluid and dispersed phases in a particle-laden turbulent channel flow with the aid of 3-D PTV. *Experiments in Fluids*, 29 (Suppl. S):S185–S193, 2000.
- A. Ten Cate, J.J. Derksen, L.M. Portella, and H.E. Van Den Akker. Fully resolved simulations of colliding monodisperse spheres in forced isotropic turbulence. *J. Fluid Mech.*, 519:233–271, 2004.
- Y. Tsuji, Y. Morikawa, and K. Terashima. Fluid-dynamic interaction between two spheres. *Int. J. Multiphase Flow*, 8(1):71–82, 1982.
- Y. Tsuji, Y. Morikawa, and H. Shiomi. LDV measurements of an air-solid two-phase flow in a vertical pipe. *J. Fluid Mech.*, 139:417–434, 1984.
- Y. Tsuji, Y. Morikawa, and Y. Fujiwara. Pipe flow with solid particles fixed in space. *Int. J. Multiphase Flow*, 11(2):177–188, 1985.
- M. Uhlmann. An immersed boundary method with direct forcing for the simulation of particulate flows. *J. Comput. Phys.*, 209(2):448–476, 2005a.
- M. Uhlmann. New results on the simulation of particulate flows. Technical Report No. 1038, CIEMAT, Madrid, Spain, 2004. ISSN 1135-9420.
- M. Uhlmann. An improved fluid-solid coupling method for DNS of particulate flow on a fixed mesh. In M. Sommerfeld, editor, *Proc. 11th Workshop Two-Phase Flow Predictions*, Merseburg, Germany, 2005b. Universität Halle. ISBN 3-86010-767-4.
- M. Uhlmann. Direct numerical simulation of sediment transport in a horizontal channel. Technical Report No. 1088, CIEMAT, Madrid, Spain, 2006a. ISSN 1135-9420.
- M. Uhlmann. Experience with DNS of particulate flow using a variant of the immersed boundary method. In P. Wesseling, E. Oñate, and J. Périaux, editors, *Proc. ECCOMAS CFD 2006*, Egmond aan Zee, The Netherlands, 2006b. TU Delft. ISBN 90-9020970-0.
- R. Verzicco and P. Orlandi. A finite-difference scheme for three-dimensional incompressible flows in cylindrical coordinates. *J. Comput. Phys.*, 123:402–414, 1996.
- L.-P. Wang and M.R. Maxey. Settling velocity and concentration distribution of heavy particles in homogeneous isotropic turbulence. *J. Fluid Mech.*, 256:27–68, 1993.
- A.M. Wood, W. Hwang, and J.K. Eaton. Preferential concentration of particles in homogeneous and isotropic turbulence. *Int. J. Multiphase Flow*, 31:1220–1230, 2005.
- J. Wu and R. Manasseh. Dynamics of dual-particles settling under gravity. *Int. J. Multiphase Flow*, 24:1343–1358, 1998.
- J.J. Wylie and D.L. Koch. Particle clustering due to hydrodynamical interactions. *Phys. Fluids*, 12(5):964–970, 2000.
- B.H. Yang, J. Wang, D.D. Joseph, H.H. Hu, T.-W. Pan, and R. Glowinski. Migration of a sphere in tube flow. *J. Fluid Mech.*, 540:109–131, 2005.
- J. Young and A. Leeming. A theory of particle deposition in turbulent pipe flow. *J. Fluid Mech.*, 340:129–159, 1997.

- M.I. Yudine. Physical considerations on heavy-particle diffusion. In *Atmospheric diffusion and air pollution*, number 6 in Adv. Geophys., pages 185–191. Academic Press, 1959.
- L. Zeng, S. Balachandar, and P. Fischer. Wall-induced forces on a rigid sphere at finite Reynolds numbers. *J. Fluid Mech.*, 536:1–25, 2005.
- L. Zeng, S. Balachandar, P. Fischer, and F. Najjar. Interaction of a stationary finite-size particle with wall-turbulence. *J. Fluid Mech.*, 2007. *(to appear)*.
- C.M. Zettner and M. Yoda. Moderate-aspect-ratio elliptical cylinders in simple shear with inertia. *J. Fluid Mech.*, 442:241–266, 2001.
- C. Zhu, S.-C. Liang, and L.-S. Fan. Particle wake effects on the drag force of an interactive particle. *Int. J. Multiphase Flow*, 20(1):117–129, 1994.

case	$\frac{\rho_p}{\rho_f}$	$ \mathbf{g} h/u_b^2$	St^+	St_b	N_p	Ω
A	10	1.625	67	3.75	512	$4h \times 2h \times h$
B	2.21	12.108	15	0.83	4096	$8h \times 2h \times 4h$

Table 1: Physical parameters used in the simulation of particulate flow in a vertical plane channel. In all cases the particle diameter is chosen as $D = h/20$, the global solid volume fraction is set to $\Phi_s = 0.0042$.

case	$N_x \times N_y \times N_z$	$\Delta t u_b / \Delta x$	$t_{obs} u_b / h$
A	$1024 \times 513 \times 256$	0.5761	700
B	$2048 \times 513 \times 1024$	0.4148	105

Table 2: Numerical parameters employed in the simulations. N_i is the number of grid nodes in the i th direction, t_{obs} is the observation interval after discarding the initial transient. The grid spacing in all cases is fixed at $\Delta x = h/256$, corresponding to $N_L = 515$ Lagrangian force points per particle.

	present results, case B			single-phase (Moser et al., 1999)		
	$S(u'_f)$	$S(v'_f)$	$S(w'_f)$	$S(u'_f)$	$S(v'_f)$	$S(w'_f)$
$y^+ = 20$	-0.948	-0.135	0.019	-0.323	-0.204	-0.006
$\bar{y} = 1$	-1.289	0.029	0.031	-0.629	0.030	-0.046

Table 3: Skewness of the pdfs of fluid velocity components at two different wall distances, compared to single-phase reference data from Moser et al. (1999).

	$S(u'_c)$	$S(v'_c)$	$S(w'_c)$
$y^+ = 17$	0.089	-1.221	0.009
$y^+ = 73$	0.038	0.003	0.022
$y^+ = 220$	0.025	0.014	0.032

Table 4: Skewness of the pdfs of particle velocity components in case B at different wall distances.

case	$T_{Lp,1} u_b / h$	$T_{Lp,2} u_b / h$	$T_{Lp,3} u_b / h$
A	13.58	0.86	2.30
B	8.15	0.48	0.79

Table 5: Integral time scales (in bulk units) computed from the Lagrangian particle velocity auto-correlations, as defined in equation (9).

$\mathcal{E}(\langle u \rangle)$	$\mathcal{E}(\sqrt{\langle u'u' \rangle})$	$\mathcal{E}(\sqrt{\langle v'v' \rangle})$	$\mathcal{E}(\sqrt{\langle w'w' \rangle})$	$\mathcal{E}(\langle u'v' \rangle)$
0.0069	0.0672	0.0213	0.0070	0.0200

Table 6: The maximum relative difference between the computation of the Eulerian statistics by averaging over the composite flow field and averaging over the fluid nodes only, estimated from 12 instantaneous flow fields. The definition of the 'error' is given in (13).

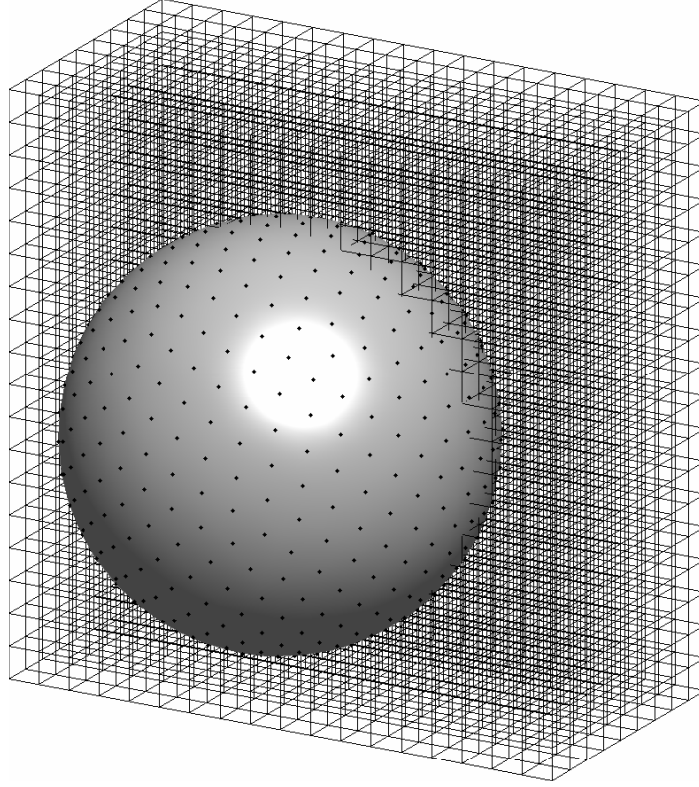


Figure 1: The Cartesian grid in the vicinity of a sphere with diameter $D/\Delta x = 12.8$, also showing the Lagrangian force points attached to its surface ($N_L = 515$).

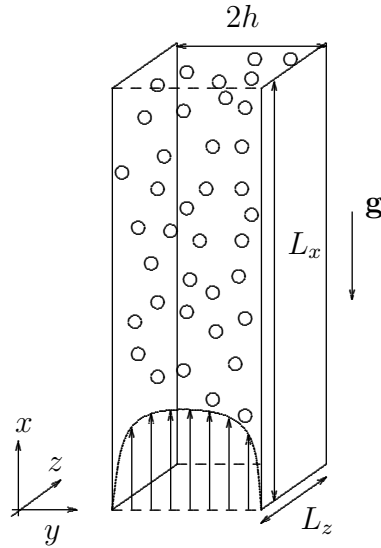


Figure 2: The geometrical configuration for vertical plane channel flow with suspended particles. The fluid motion is induced by a negative mean pressure gradient in the direction of the x coordinate. The computational domain is periodic in x and z .

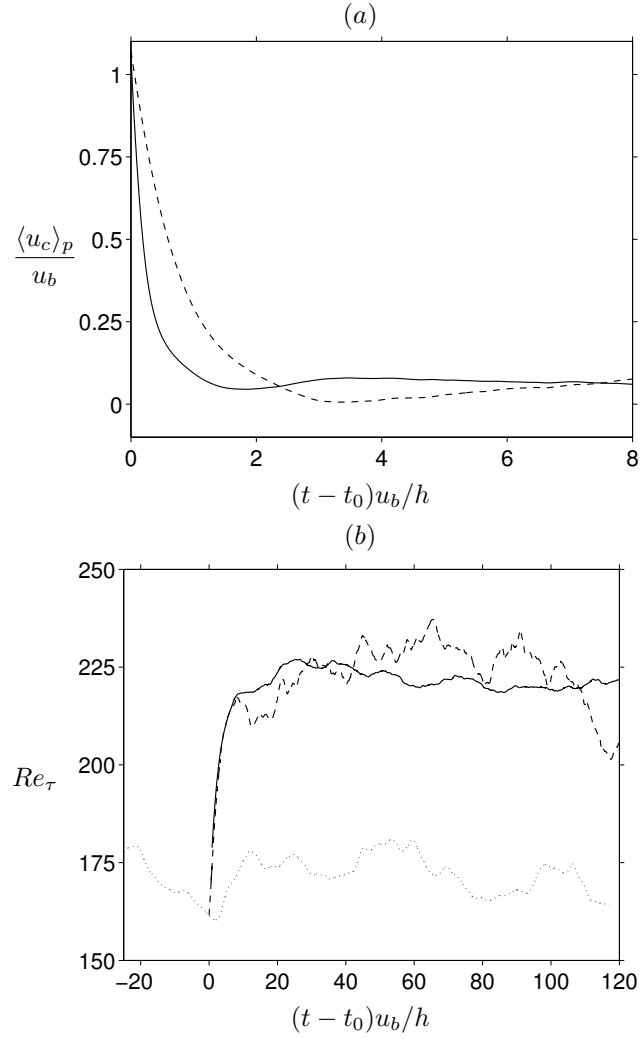


Figure 3: (a) The average vertical particle velocity during start-up of the two-phase simulation. (b) The time evolution of the friction-velocity-based Reynolds number around the start-up time. Particles are added at $t = t_0$. ---- case A; — case B; single-phase flow.

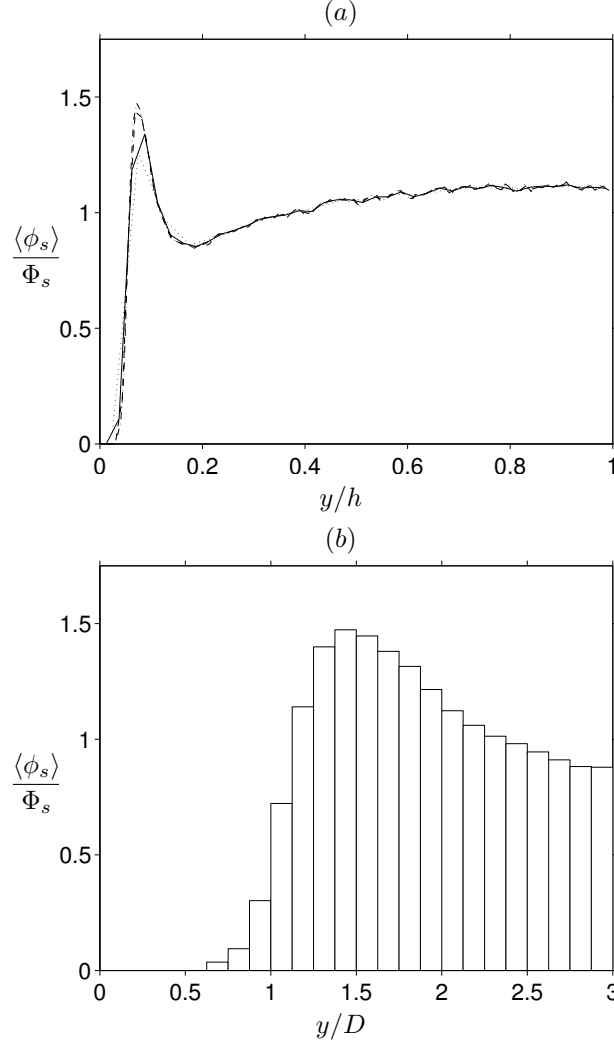


Figure 4: The effect of discrete binning upon the data for the mean solid volume fraction $\langle \phi_s \rangle$ in case B. (a) Profiles accumulated for different numbers of bins: $\cdots \cdots \cdots N_{bin} = 40$; $\text{---} N_{bin} = 80$; $\text{----} N_{bin} = 160$; $\text{--}\cdot\text{--} N_{bin} = 320$. (b) The data for $N_{bin} = 320$ in a close-up near the wall; the abscissa is normalized with the particle diameter.

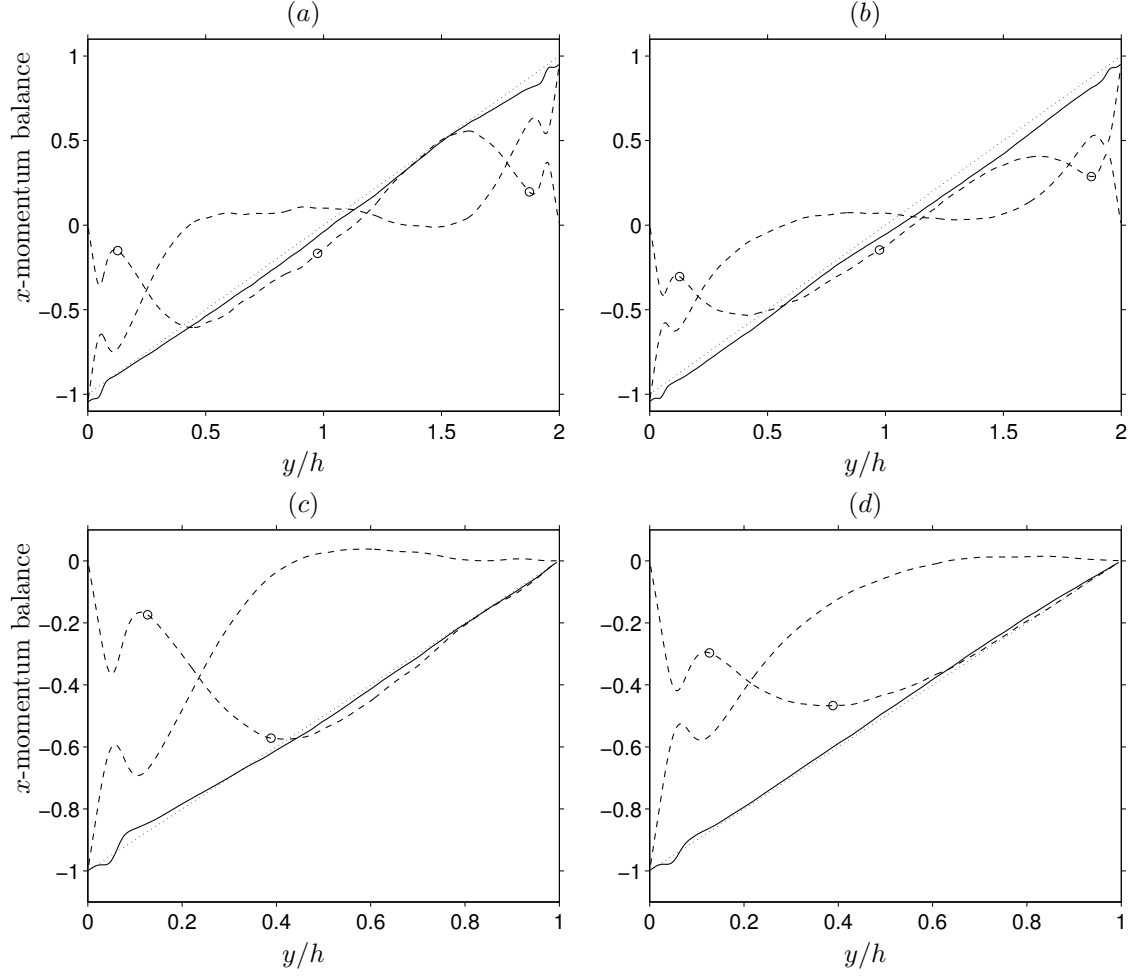


Figure 5: The integral of the averaged streamwise momentum equation (6), evaluated from the statistical data accumulated over the observation interval in cases A (*a* and *c*) and B (*b,d*). (*a*), (*b*) show the full channel width; in (*c*),(*d*) the data is averaged over both channel half-widths, invoking odd symmetry. Statistics were accumulated over the composite flow field. The lines correspond to: — $\tau_{tot} + I_\phi$; ---- τ_{tot} ; - - \circ - - I_ϕ ; $y/h - 1$.

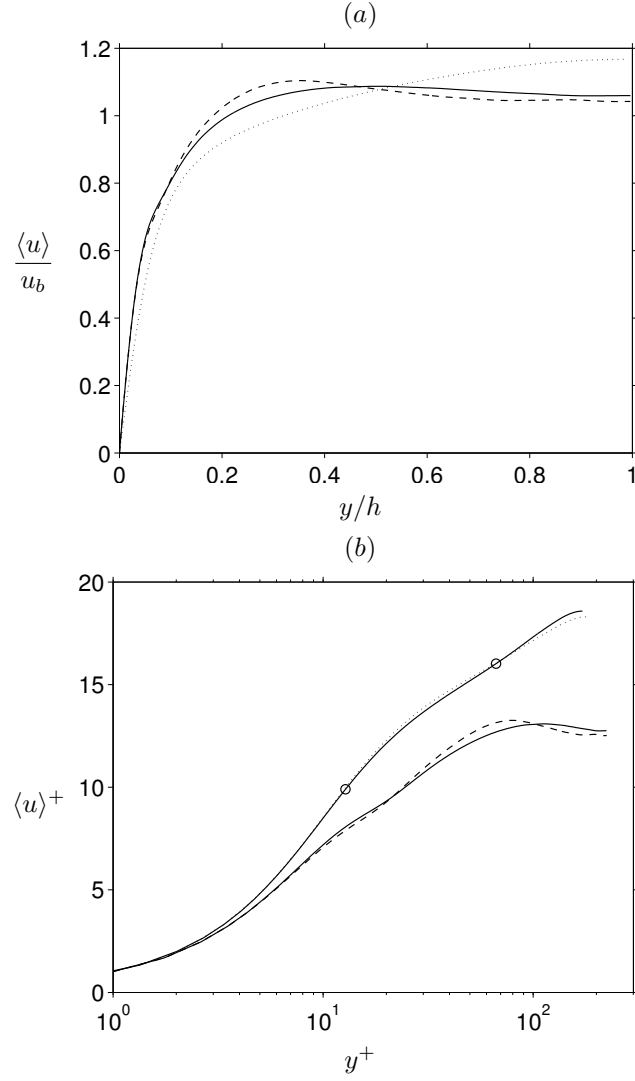


Figure 6: Wall-normal profiles of the mean fluid velocity, (a) in outer units, (b) in wall units: ---- case A; — case B; single phase flow (Kim et al., 1987). Statistics were accumulated over the composite flow field. In (b) —○— indicates the result of the single-phase computation with our code using the domain size of case A.

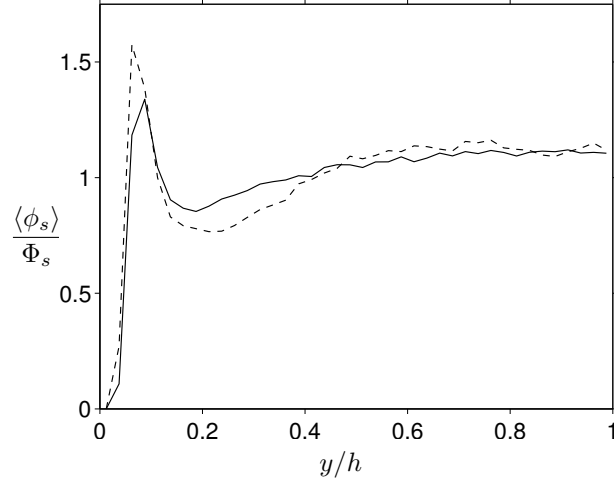


Figure 7: The wall-normal profile of the mean solid volume fraction for case A (----) and case B (—), using $N_{bin} = 80$.

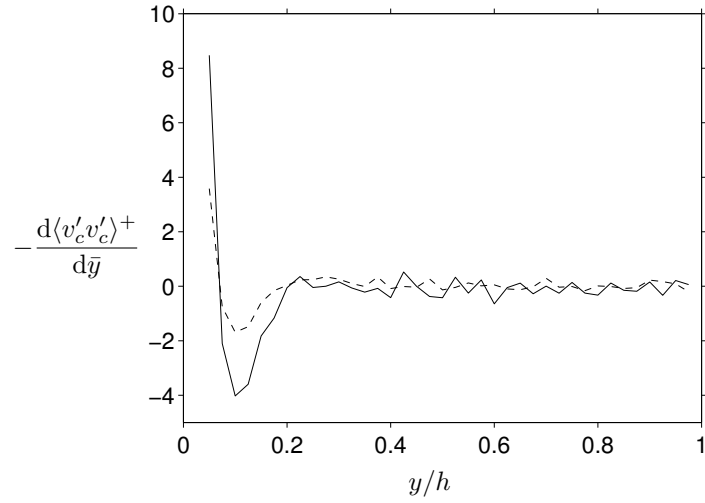


Figure 8: Wall-normal profiles of the derivative of the wall-normal particle velocity correlation; ---- case A; — case B.

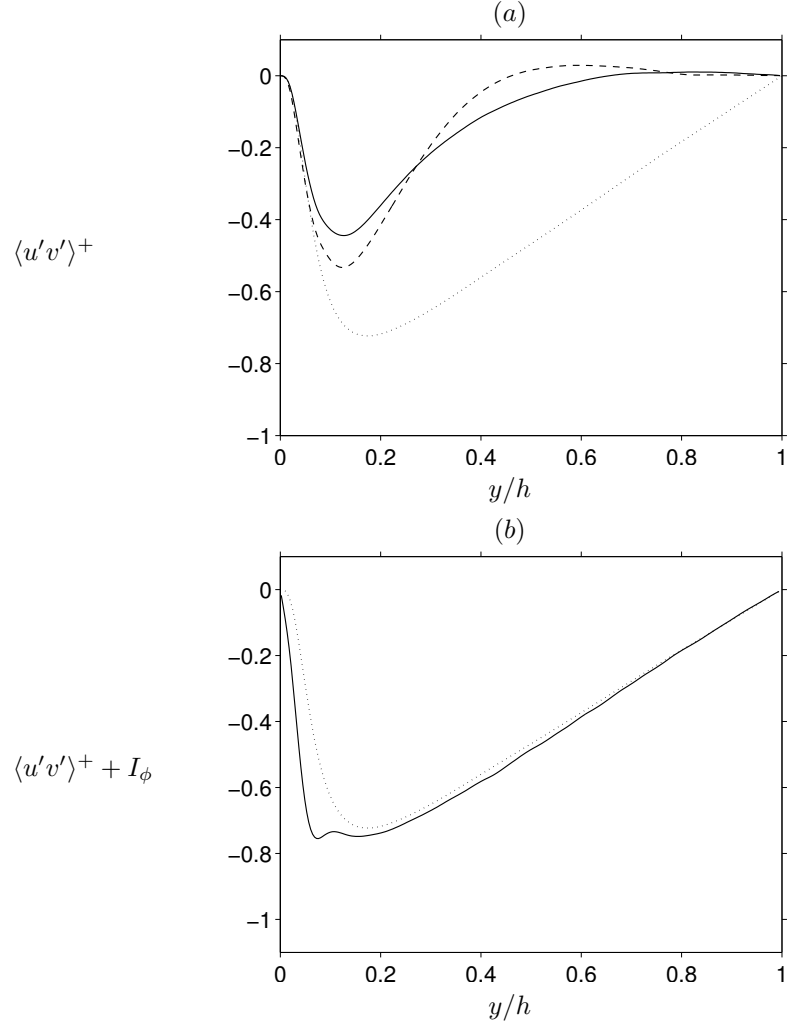


Figure 9: (a) Wall-normal profiles of the Reynolds shear stress; line styles as in figure 6. In (b) The sum of the Reynolds shear stress and the particle contribution to equation (6), $\langle u'v' \rangle^+ + I_\phi$, for case B (—) is compared to the Reynolds shear stress of the single-phase flow (·····). Statistics were accumulated over the composite flow field.

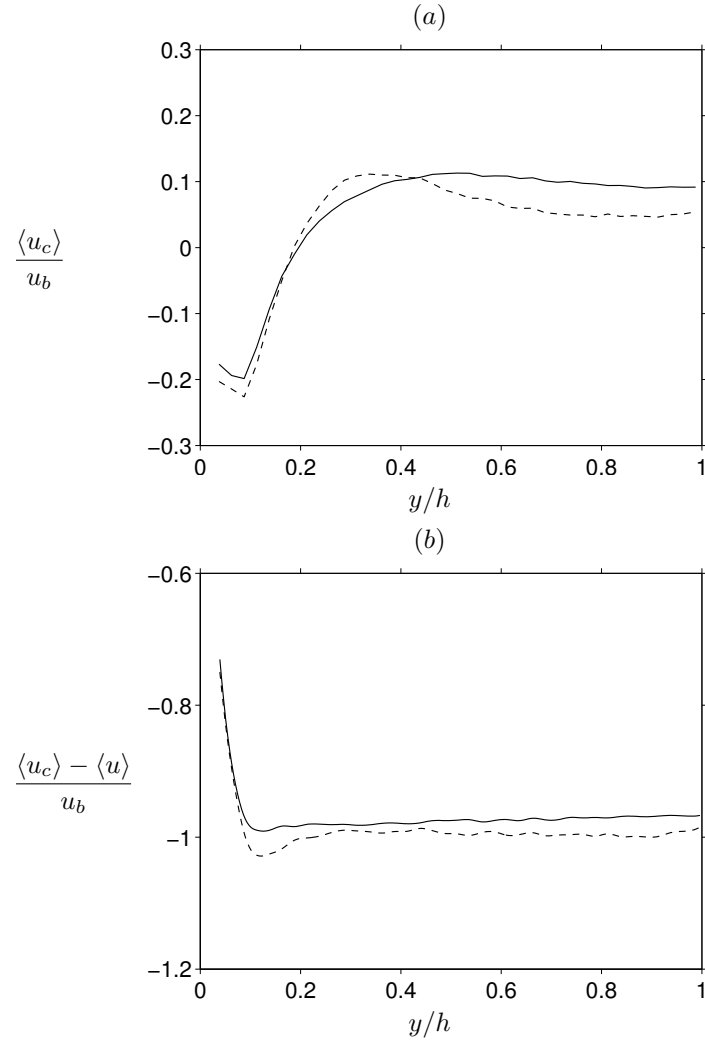


Figure 10: Wall-normal profiles of (a) the mean particle velocity, and (b) the difference between the mean velocities of the two phases: ---- case A; — case B. Statistics for $\langle u \rangle$ were accumulated over the composite flow field.

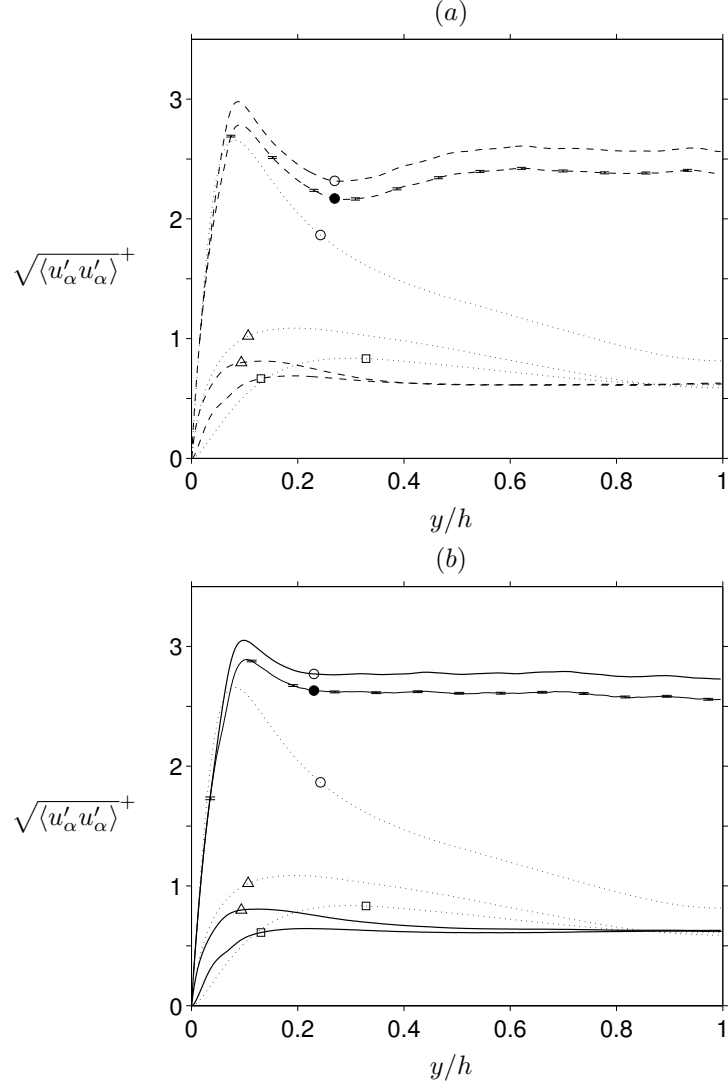


Figure 11: Wall-normal profiles of the r.m.s. fluid velocity fluctuations; line styles as in figure 6. (a) Data from case A vs. single-phase flow; (b) case B vs. single-phase flow. The coordinate directions are indicated by the symbols: \circ $\alpha = 1$; \square $\alpha = 2$; \triangle $\alpha = 3$. The lines with the symbol “ \bullet ” indicate the profiles of the streamwise component, corrected for the overestimation due to the accumulation of statistics over the composite flow field (cf. appendix A); errorbars show the standard deviation of the fit.

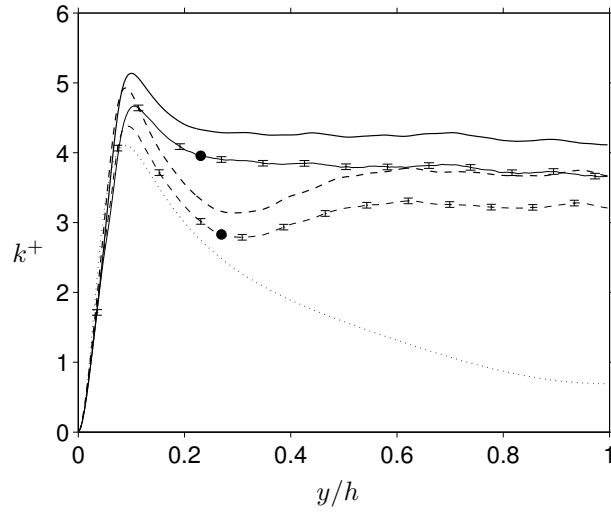


Figure 12: Wall-normal profiles of the turbulent kinetic energy $k = \sum_{i=1}^3 \langle u'_i u'_i \rangle / 2$; line styles as in figure 6. The lines with the symbol “•” indicate the profiles corrected for the overestimation of the streamwise stress component, due to the accumulation of statistics over the composite flow field (cf. appendix A); errorbars show the standard deviation of the fit.

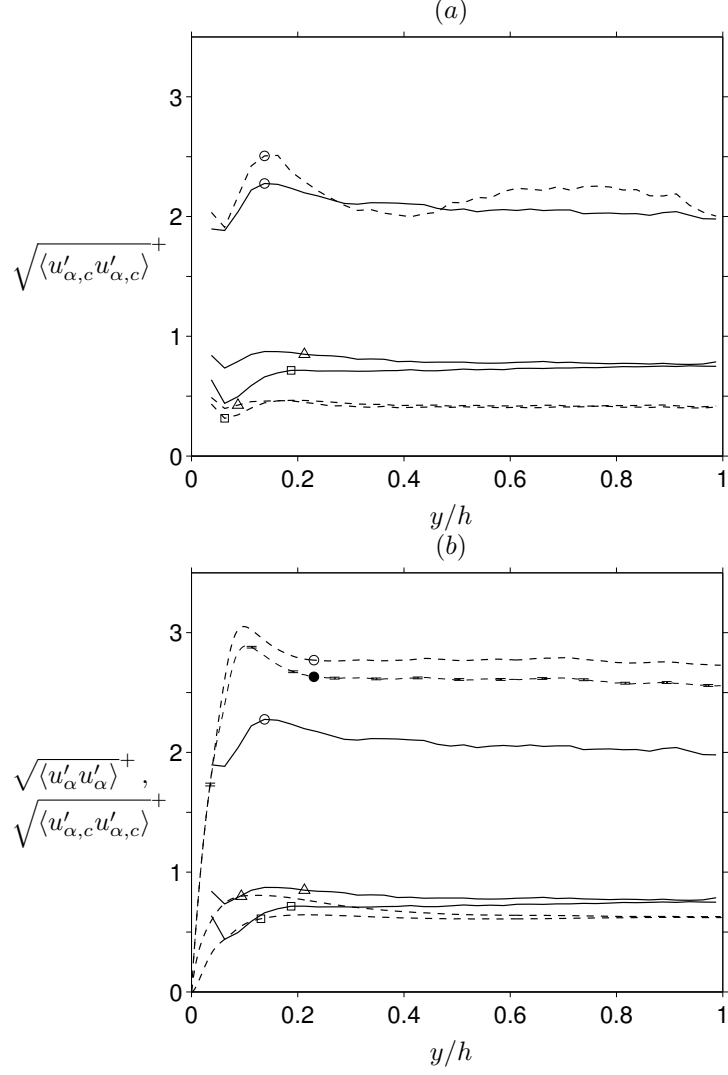


Figure 13: Wall-normal profiles of the r.m.s. particle velocity fluctuations: (a) case A vs. case B with line styles as in figure 10; (b) data of case B (solid lines) compared to the r.m.s. fluid velocity (dashed lines). The coordinate directions are indicated by the symbols: \circ $\alpha = 1$; \square $\alpha = 2$; \triangle $\alpha = 3$. In (b) the dashed line with the symbol “•” indicates the profile of the streamwise fluid velocity component, corrected for the overestimation due to the accumulation of statistics over the composite flow field (cf. appendix A); errorbars show the standard deviation of the fit.

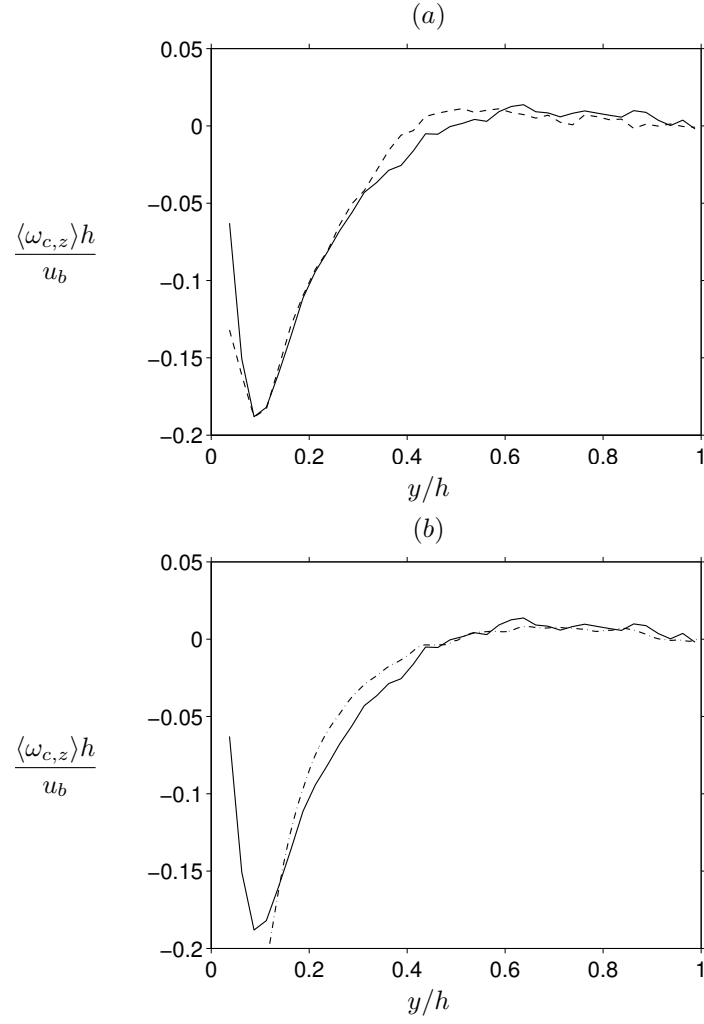


Figure 14: Wall-normal profiles of the mean angular particle velocity; line styles as in figure 10. In (b) the data for case B is compared to the formula $-0.1 \cdot d\langle u \rangle / dy$ (— · —).

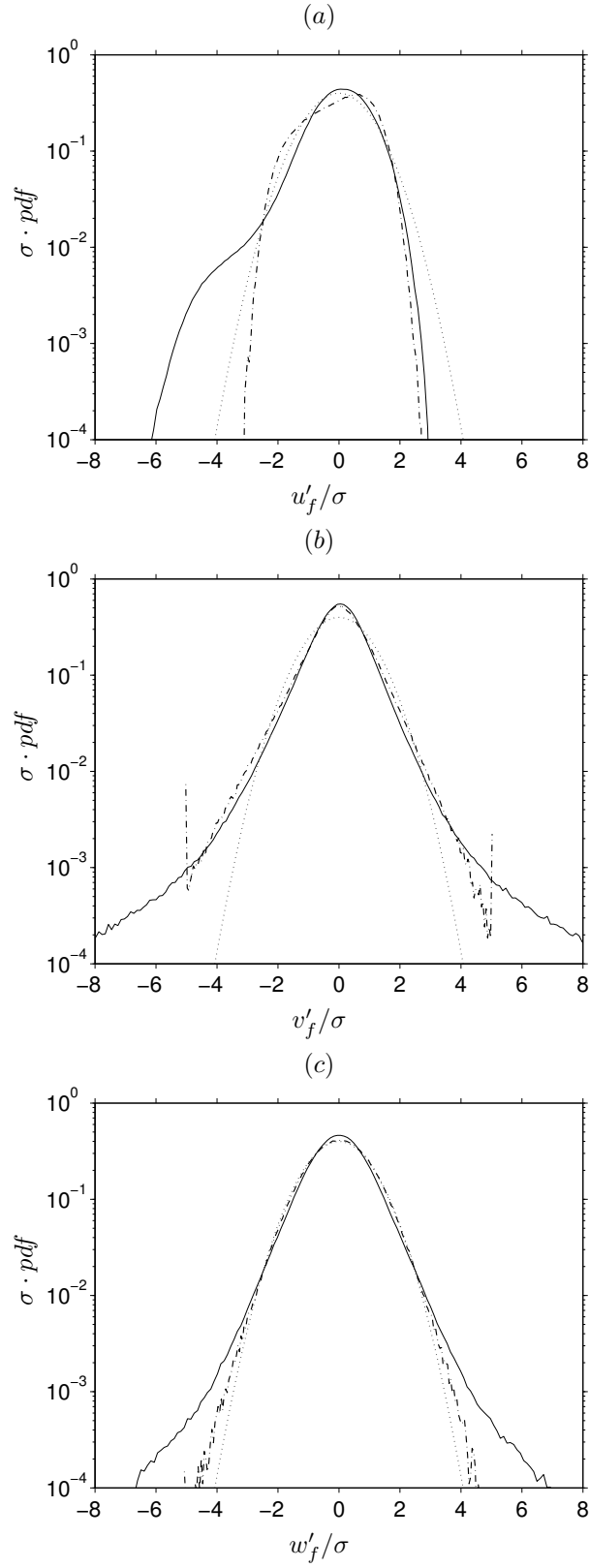


Figure 15: Normalized probability density functions of fluid velocity components, computed from 12 instantaneous flow fields of case B (taking into account only nodes inside the fluid domain) at $y^+ = 20$: (a) streamwise, (b) wall-normal, and (c) spanwise; — present results (case B); - - - single-phase data from Moser et al. (1999) at $Re_\tau = 180$; Gaussian reference curve.

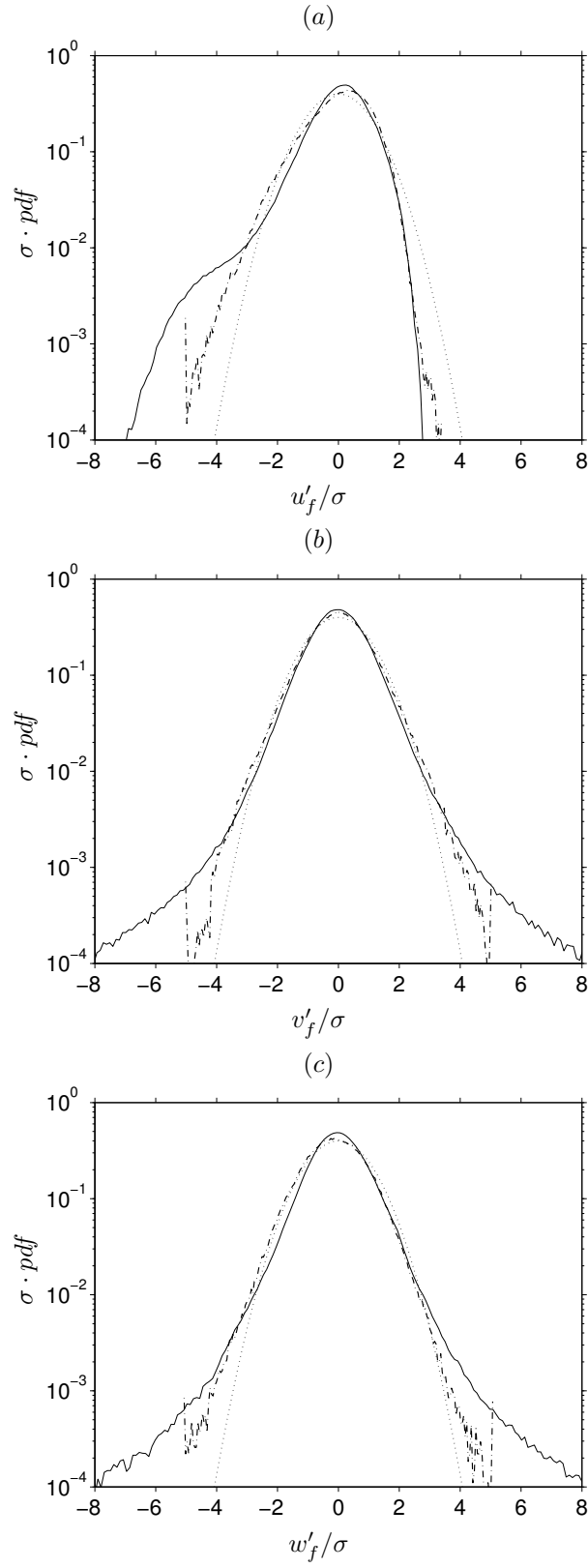


Figure 16: As figure 15, but for the center of the channel ($y/h = 1$).

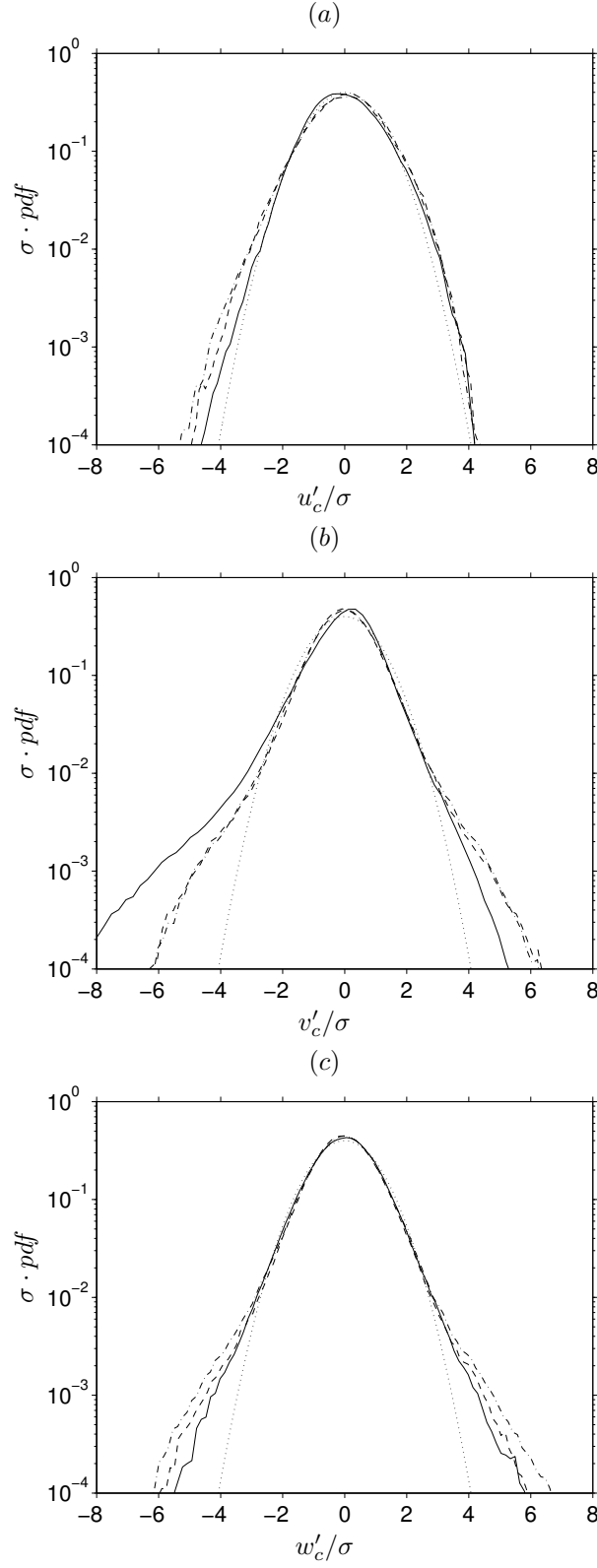


Figure 17: Normalized probability density functions of particle velocity components in case B at different wall-distances: — $y^+ = 17$; ---- $y^+ = 73$; - · - $y^+ = 220$; Gaussian reference curve.

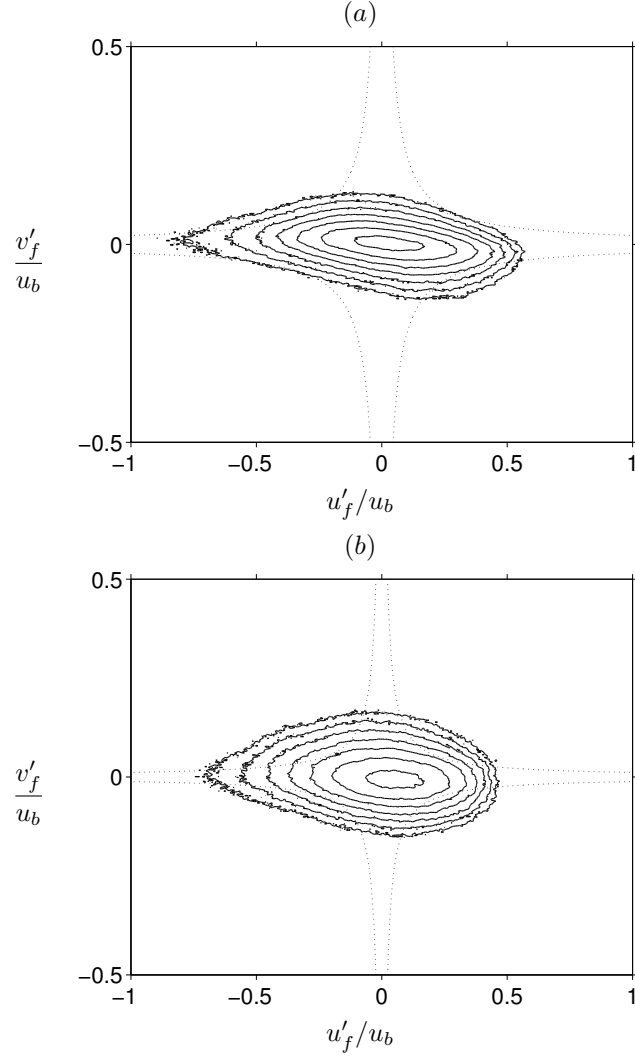


Figure 18: Isocontours of the joint probability density function of streamwise and wall-normal fluid velocity fluctuations in case B (evaluated from 12 instantaneous flow fields, taking into account only points in the fluid domain). The values for the contours vary between 0.0125 and 0.8 of the maximum probability, increasing by a factor of 2 between each level. (a) $y^+ = 20$; (b) $y^+ = 74$. The dotted lines indicate $|u'_f v'_f| = -8\langle u'_f v'_f \rangle$.

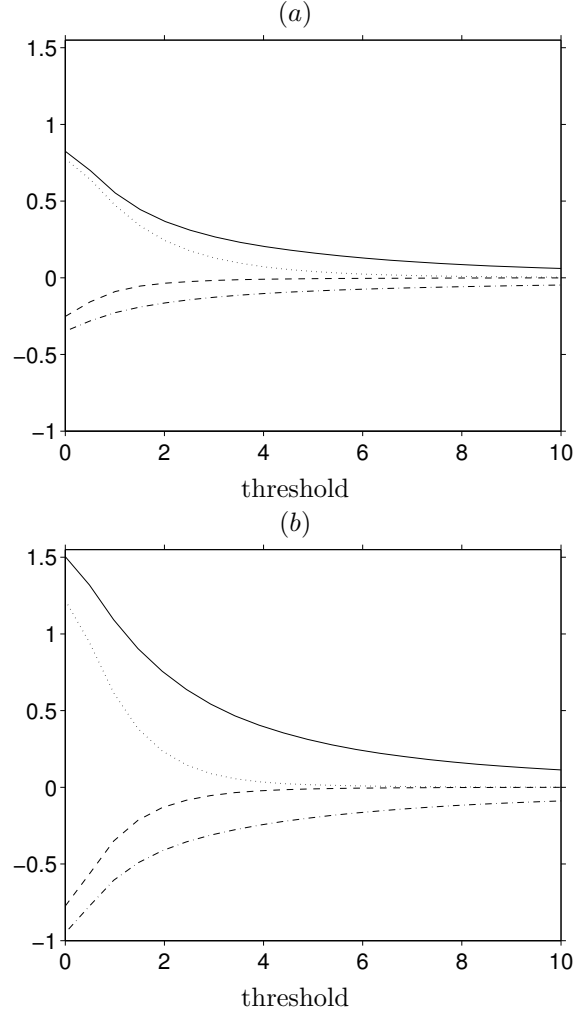


Figure 19: Fractional contribution from each quadrant to the Reynolds shear stress as a function of threshold: ----, first; —, second; — · —, third; ·····, fourth. (a) $y^+ = 20$; (b) $y^+ = 74$. The threshold is normalized by the r.m.s. intensities of each plane: $\sqrt{\langle u'_f u'_f \rangle} \cdot \sqrt{\langle v'_f v'_f \rangle}$.

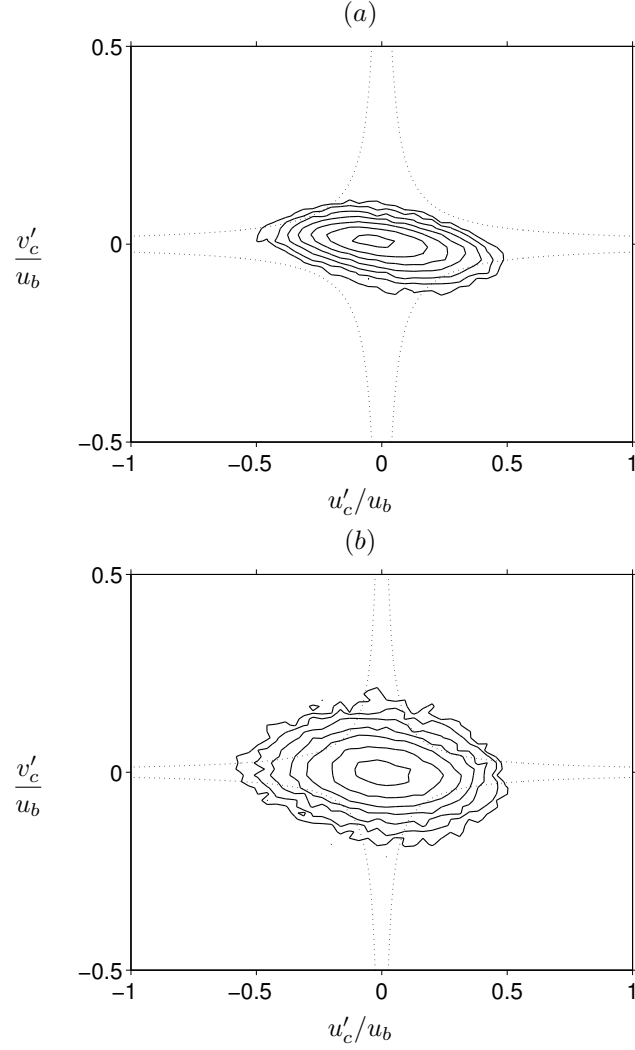


Figure 20: Isocontours of the joint probability density function of streamwise and wall-normal particle velocity fluctuations in case B (evaluated from 250 instantaneous particle distributions). The values for the contours vary between 0.0125 and 0.8 of the maximum, increasing by a factor of 2 between each level. (a) wall-normal bin centered at $y^+ = 17$; (b) $y^+ = 73$. The dotted lines indicate $|u'_c v'_c| = -8\langle u'_c v'_c \rangle$.

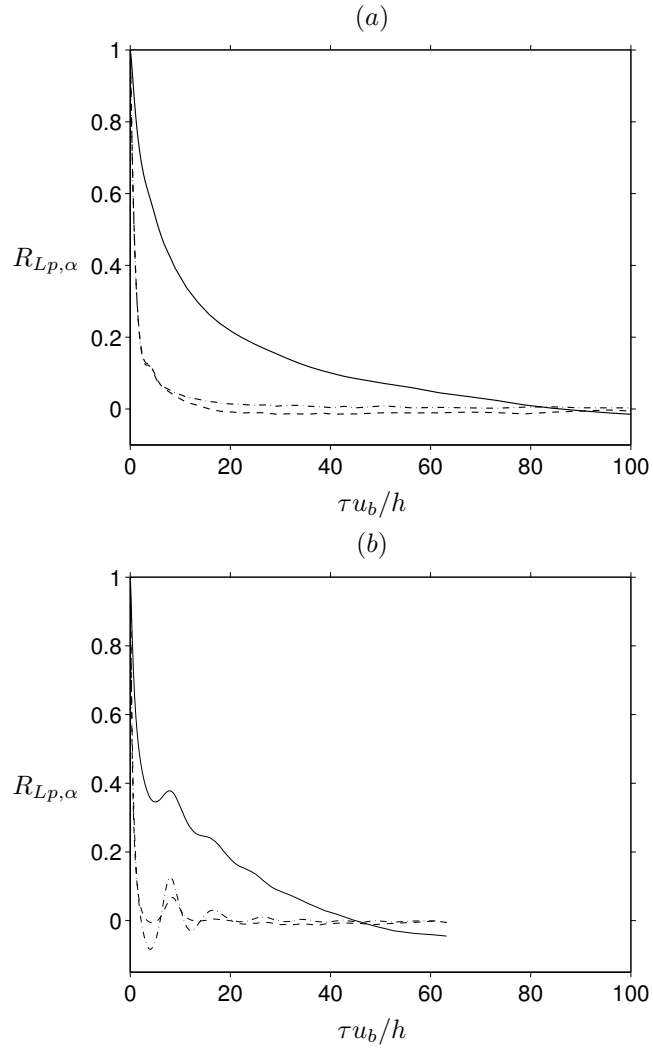


Figure 21: Lagrangian particle velocity auto-correlations as a function of the separation time τ : (a) case A; (b) for case B. — $\alpha = 1$; ---- $\alpha = 2$; - · - $\alpha = 3$.

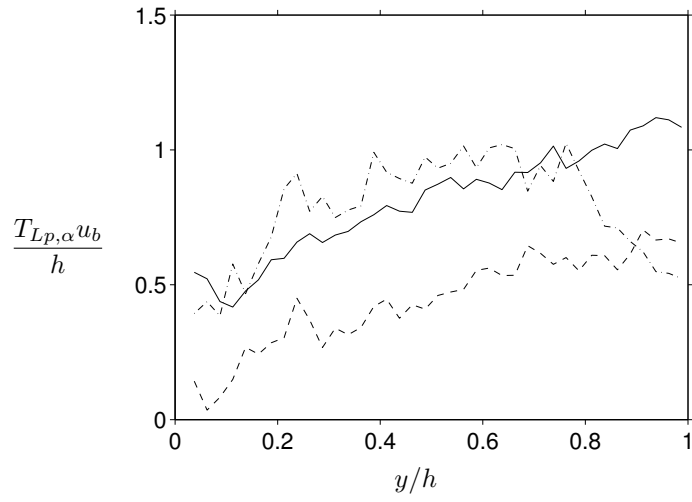


Figure 22: Integral time scales (in bulk units) computed from the Lagrangian particle velocity auto-correlations as a function of the particle's wall-distance at the initial time, case B. — $0.1 \cdot T_{Lp,1} u_b / h$; ---- $T_{Lp,2} u_b / h$; - · - $T_{Lp,3} u_b / h$. Please note the scaling factor applied to the data of the streamwise component.

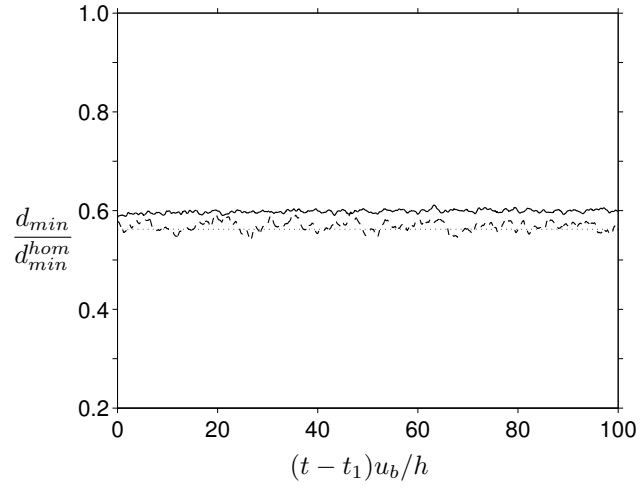


Figure 23: Time evolution of the average distance to the nearest neighbor, normalized by the value for a homogeneous distribution. Symbols as in figure 10; t_1 marks the beginning of the observation interval. The dashed line corresponds to the value for a random distribution with the same solid volume fraction (computed for 524288 particles and correspondingly streamwise extended domain).

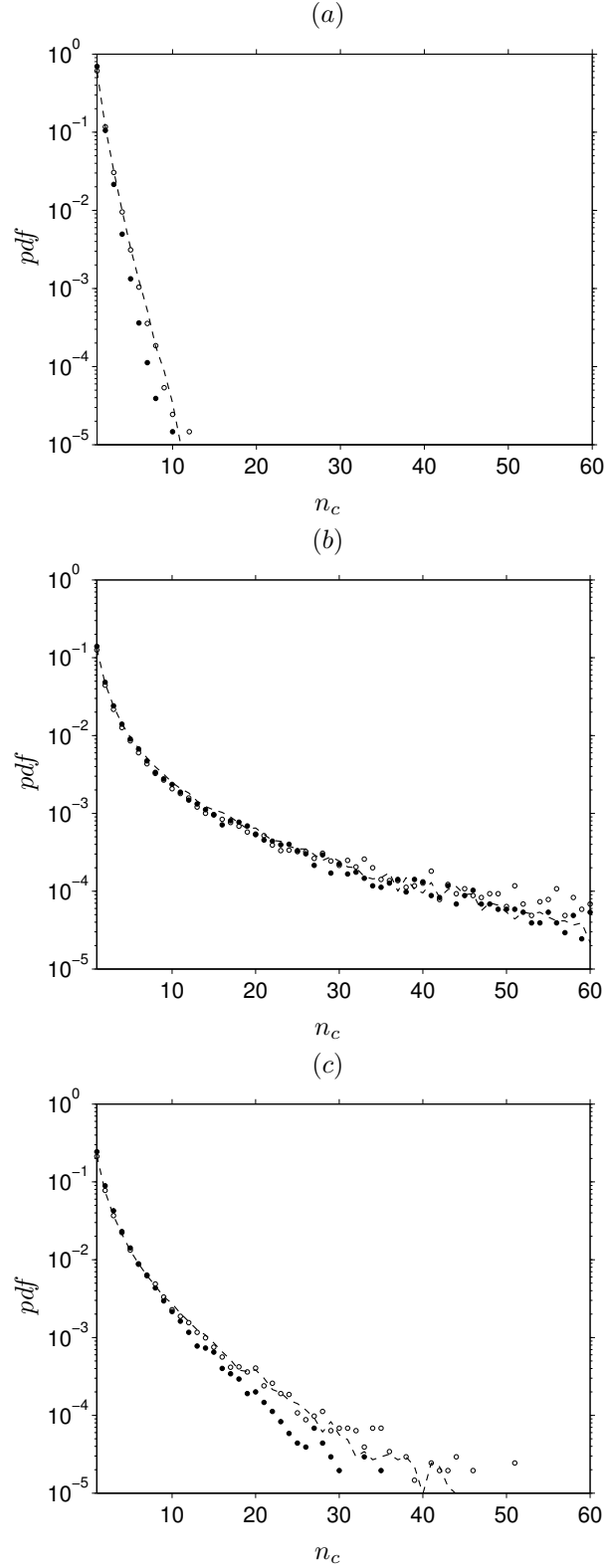


Figure 24: Probability density function of the occurrence of particle clusters with n_c members in cases A (\circ) and B (\bullet). The graphs correspond to different cut-off lengths: (a) spherical cut-off $l_c = 2.5D$; (b) spherical cut-off $l_c = 4D$; (c) elliptical cut-off with axes of length $l_{cx} = 7.5D$, $l_{cy} = l_{cz} = 2.5D$. The probability was evaluated from 400 (50) instantaneous particle distributions in case A (B), spanning the respective observation intervals. The dashed lines correspond to the probability for a random distribution of particles with the same solid volume fraction, evaluated from 100 realizations.

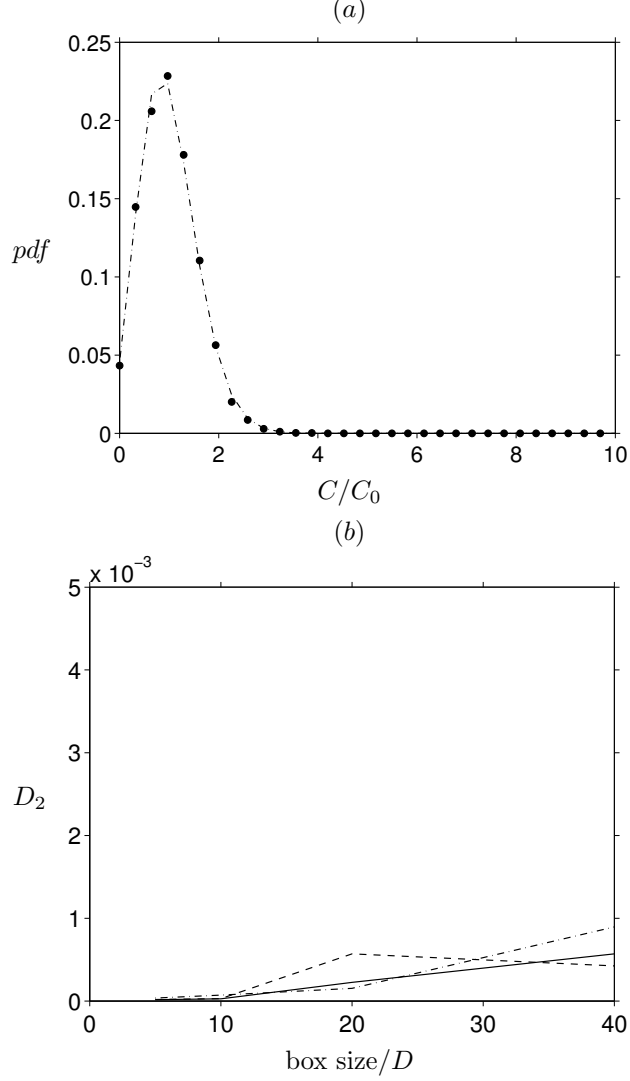


Figure 25: Local concentration of particles in case B. (a) Probability density function of the number of particles per box of size $20D \times D \times 20D$ at a wall distance of $y^+ = 28$: DNS results (\bullet) versus Poisson distribution ($-\cdot-$); C_0 is the average number of particles per box in the current y-slab. (b) The deviation between the pdf of the DNS data and the Poisson distribution according to the definition (12), plotted as a function of the linear box dimension (in the directions of the x and z coordinate): $—$ $y^+ = 28$; $----$ $y^+ = 73$; $-\cdot-$ $y^+ = 220$.

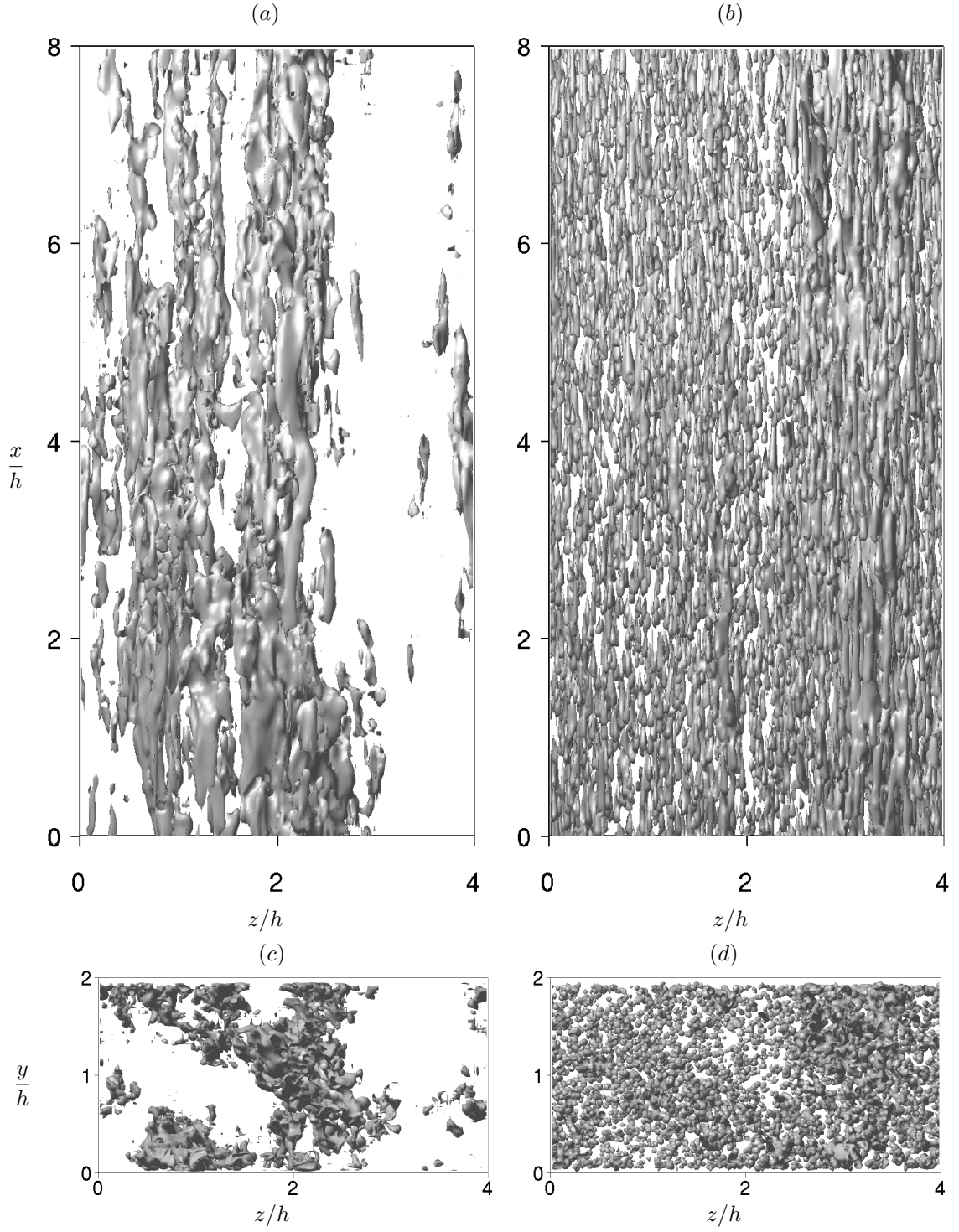


Figure 26: Instantaneous three-dimensional isosurfaces of streamwise velocity fluctuations $u' = \pm 3.6u_\tau$ (equivalent to $\pm 0.3u_b$) of case B. The graphs (a, c) show surfaces corresponding to positive values, (b, d) show negative-valued surfaces. The view in (a, b) is into the wall, in (c, d) it is in the mean flow direction. Please note that only every eighth grid point in each direction was used. Here and in figures 28, 29, 30 the full computational domain is shown.

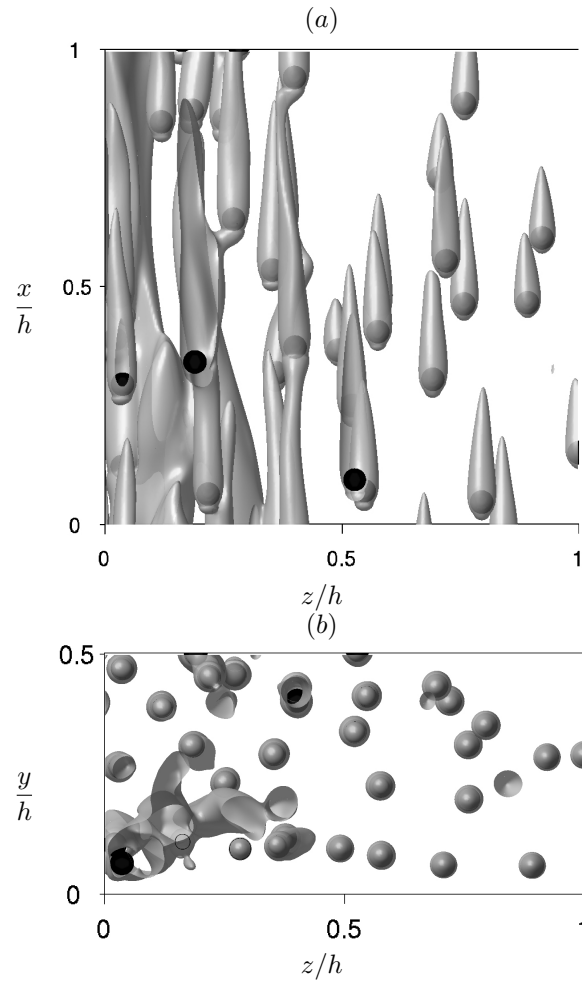


Figure 27: The same negative-valued isosurfaces as in figure 26(b, d), but shown in the sub-domain $[0, h] \times [0, 0.5h] \times [0, h]$. In addition, the particles are indicated by black spheres.

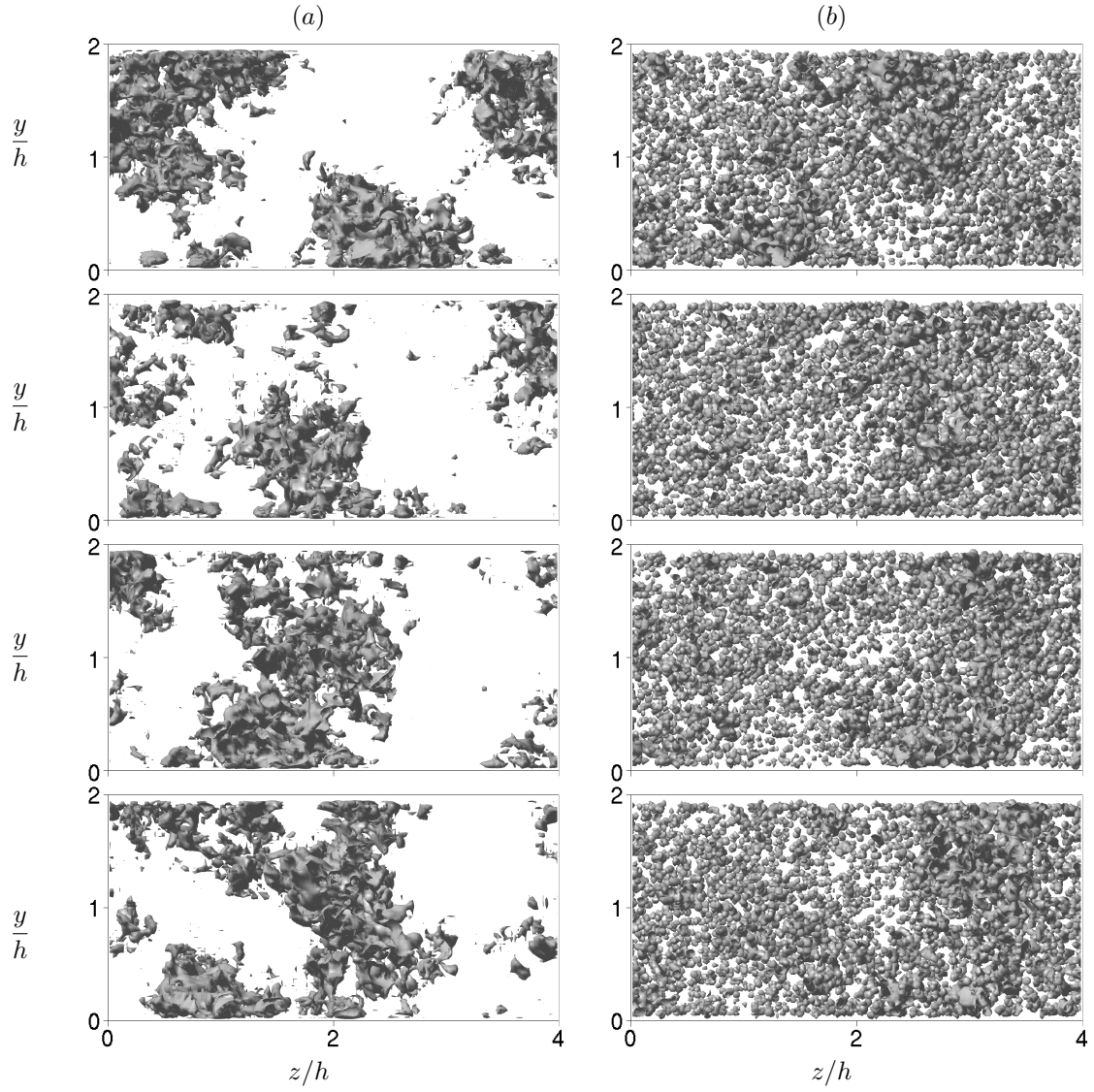


Figure 28: Isosurfaces of $u' = \pm 3.6u_\tau$ in the cross-stream plane for successive snapshots with time increasing from top to bottom by increments of approximately $14.9h/u_b$. Positive-valued surfaces are shown in (a), negative ones in (b). The plots in the last row are identical to those in figure 26(c, d).

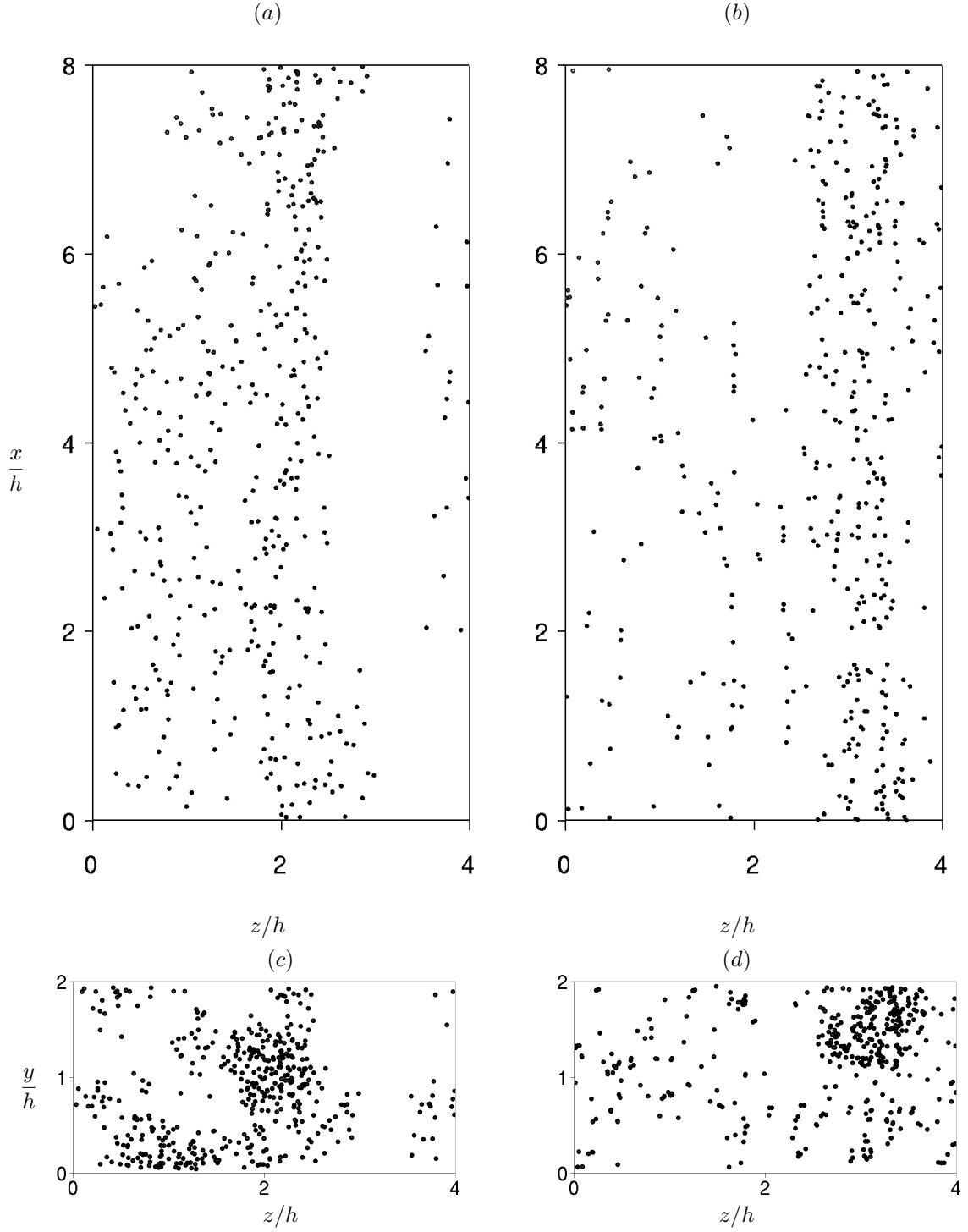


Figure 29: Instantaneous positions of particles sorted according to their streamwise velocity fluctuation: (a) $u'_c \geq +0.2u_b$; (b) $u'_c \leq -0.2u_b$. The field corresponds to the one shown in figure 26.

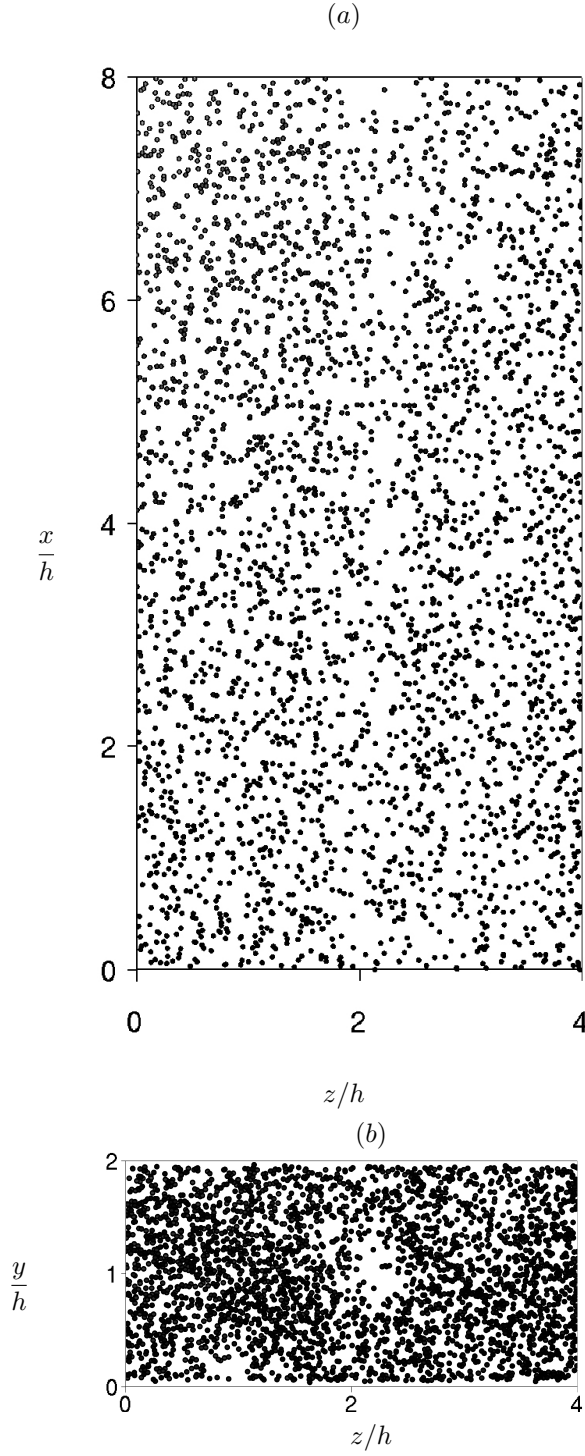


Figure 30: As figure 29, but showing particles with a streamwise velocity close to the average value, i.e. for which $-0.2u_b < u'_c < +0.2u_b$.

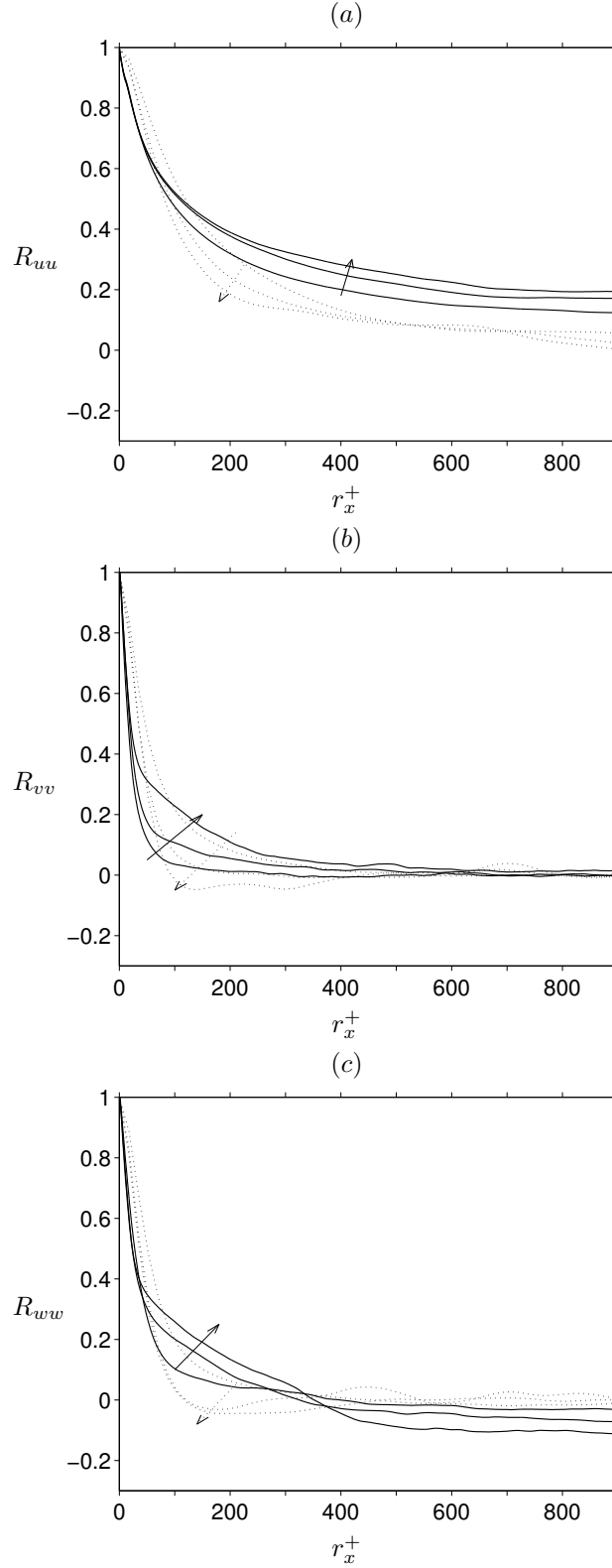


Figure 31: Two-point autocorrelations of fluid velocity fluctuations for streamwise separations, case B (evaluated from 12 instantaneous flow fields, taking into account only points in the fluid domain). The graphs show the following components of velocity: (a) streamwise, (b) wall-normal, (c) spanwise. The lines correspond to $y^+ = \{21, 87, 225\}$, increasing along the arrows. The single-phase results of Kim et al. (1987) are indicated by the dotted lines.

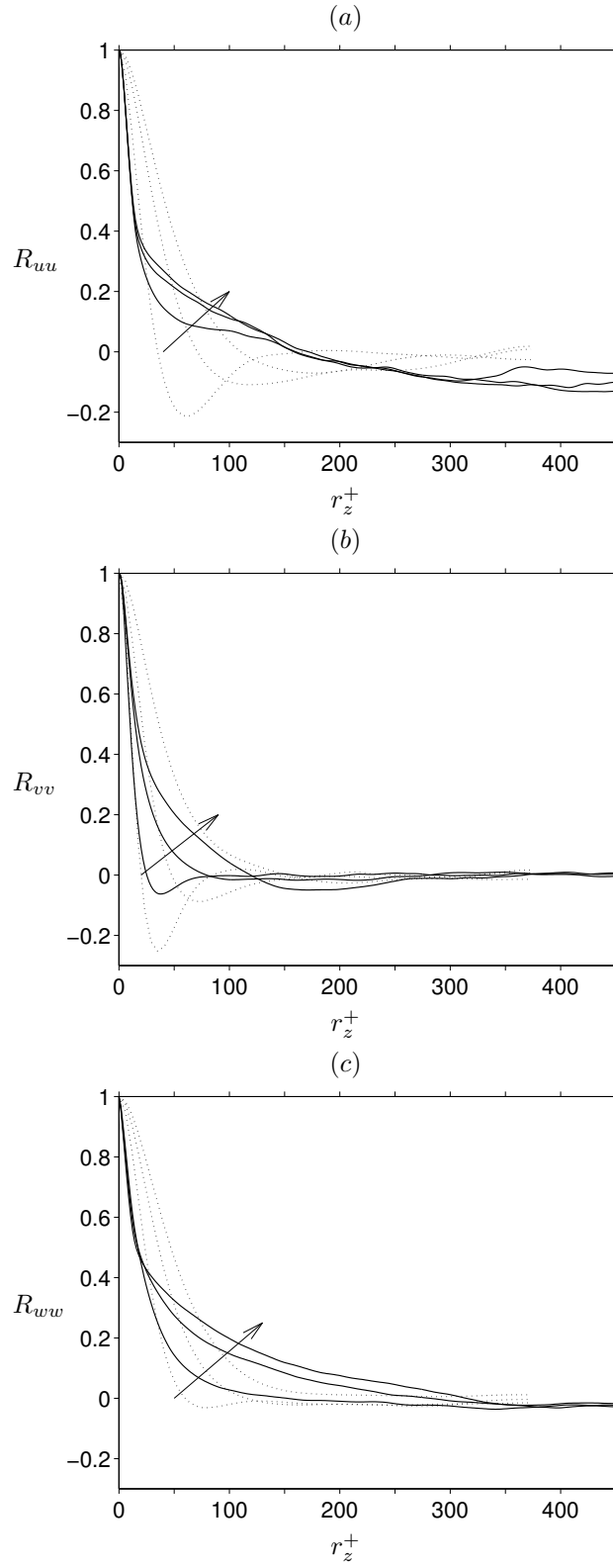


Figure 32: As figure 31, but for spanwise separations.

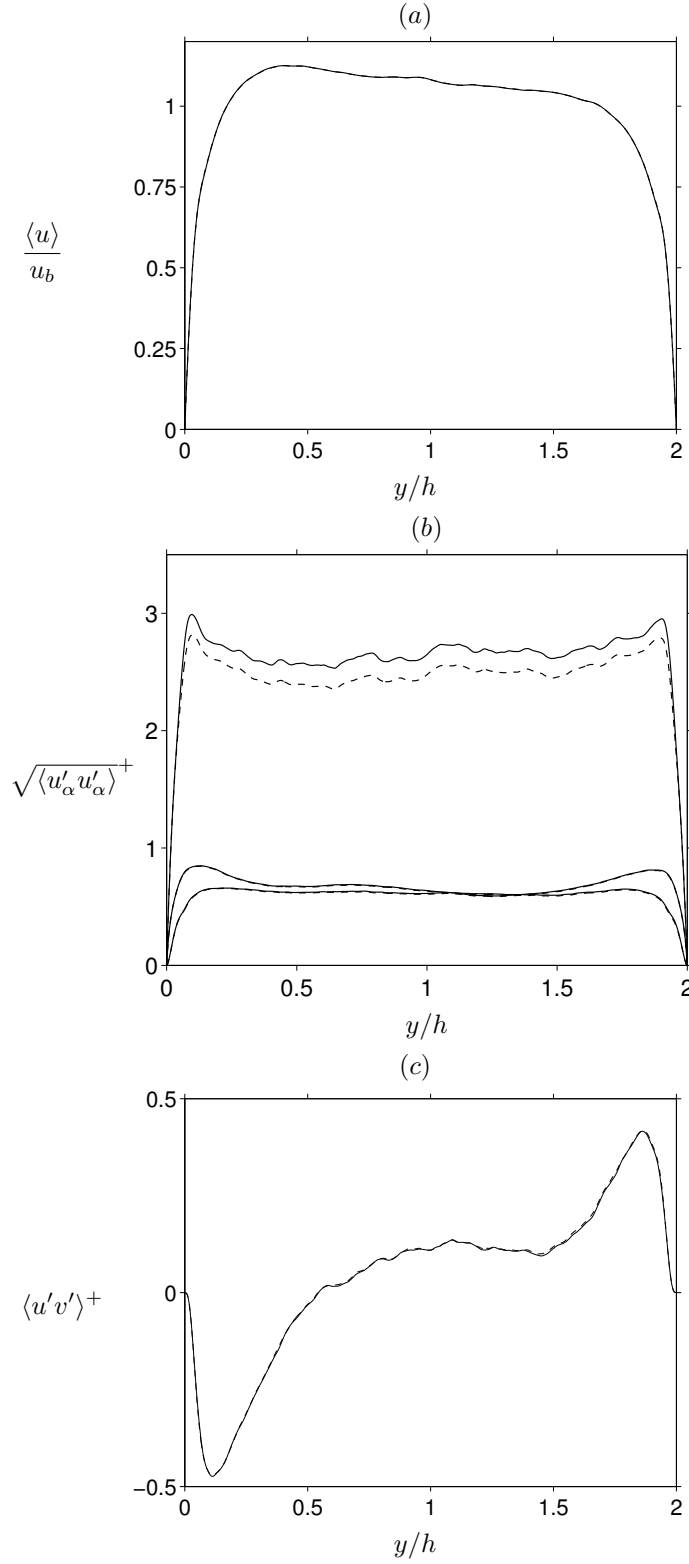


Figure 33: Eulerian statistics of case B, computed from 12 snapshots of the flow field by using two different methods: — averaging over the composite field (including fluid and solid nodes); ----, averaging over the fluid nodes only. (a) The wall-normal profile of the mean velocity, (b) the r.m.s. velocity fluctuations, (c) the Reynolds shear stress.

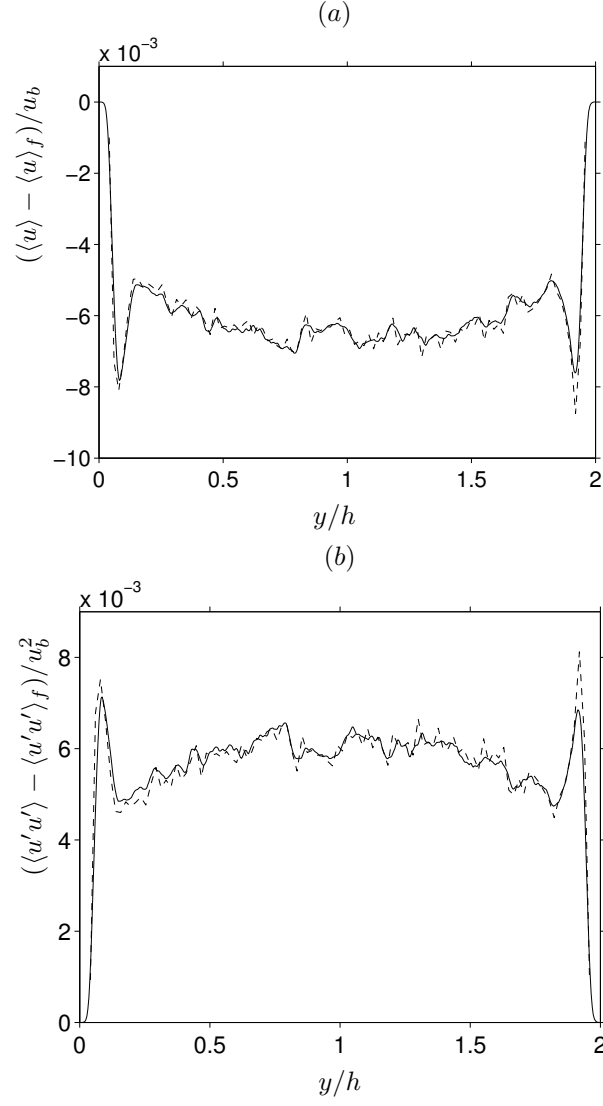


Figure 34: The difference between the two procedures of accumulating the statistics shown in figure 33: (a) the mean velocity difference; (b) the streamwise normal stress component. The dashed lines indicate the proportionality with the profile of the solid volume fraction $C \cdot \langle \phi_s \rangle(y)$, where $C = \{-1.4682, 1.3634\}$ in (a) and (b), respectively, was obtained by a least-squares fit.

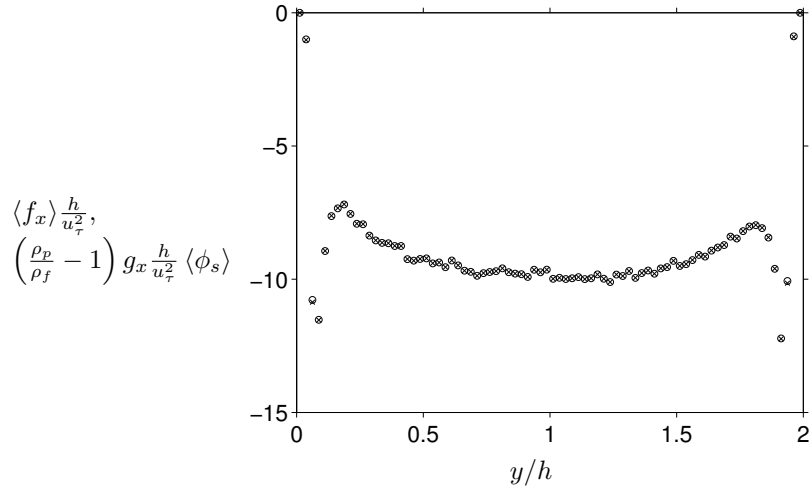


Figure 35: Wall-normal profiles of the mean streamwise force density (o) and the mean buoyancy term (x) for case B.